

REVIEW ARTICLE

Research progress on prostate-specific
membrane antigen-targeted small-molecule
radioligandsDezhao Zhang^{1,2}, Yeting Zheng², Xinyue Ge², Chun Zhang¹, and Feihu Guo^{2*}¹Department of Medicinal Chemistry, School of Pharmaceutical Science and Technology, Tianjin University, Tianjin, China²Tianjin Hengrui Pharmaceuticals Co., Ltd., Tianjin, China

Abstract

Prostate-specific membrane antigen (PSMA) is markedly overexpressed on prostate cancer cell membranes—particularly in advanced, metastatic, and metastatic castration-resistant prostate cancer (mCRPC) lesions—but is present at only low levels in healthy tissues and organs, such as the salivary glands, kidneys, and proximal small intestine. This unique characteristic makes PSMA a highly promising target for precision radiopharmaceutical-based theranostics of prostate cancer. In recent years, the rapid development of radionuclides, such as ⁶⁸Ga, ¹⁸F, ⁹⁰Y, ⁶⁴Cu, ¹⁷⁷Lu, and ²²⁵Ac, together with continuous advances in bifunctional chelators including 1,4,7,10-tetraazacyclododecane-1,4,7,10-tetraacetic acid (DOTA) and 1,4,7-triazacyclononane-1,4,7-triacetic acid (NOTA), has enabled a seamless transition from diagnosis to therapy for targeted radiotheranostic strategies. Notably, [¹⁷⁷Lu] Lu-PSMA-617 (brand name: Pluvicto) has been approved by the United States Food and Drug Administration for the treatment of patients with PSMA-positive mCRPC based on the groundbreaking findings from the Phase III VISION trial, which has fundamentally transformed the treatment landscape of this disease. Nevertheless, current PSMA-targeted radiopharmaceuticals still face multiple challenges: temporal and spatial heterogeneity of tumor PSMA expression, mechanisms of acquired drug resistance, and adverse reactions induced by dose-limiting toxicities. This review systematically reviews the latest preclinical advances and clinical translation outcomes of PSMA-targeted ligands, covering molecular design strategies, optimization of pharmacokinetic profiles, exploration of novel radionuclides, and evaluation of radiopharmaceuticals. It aims to provide a valuable reference for researchers engaged in PSMA-targeted theranostic studies.

*Corresponding author:

Feihu Guo
(feihu.guo@hengrui.com)

Citation: Zhang D, Zheng Y, Ge X, Zhang C, Guo F. Research progress on prostate-specific membrane antigen-targeted small-molecule radioligands. *Adv Radiother Nucl Med.* 2026;4(2):026180015. doi: 10.36922/ARNM026180015

Received: April 30, 2026**Revised:** June 1, 2026**Accepted:** June 15, 2026**Published online:** June 26, 2026

Copyright: © 2026 Author(s). This is an Open-Access article distributed under the terms of the Creative Commons Attribution License, permitting distribution, and reproduction in any medium, provided the original work is properly cited.

Publisher's Note: AccScience Publishing remains neutral with regard to jurisdictional claims in published maps and institutional affiliations.

Keywords: Radiopharmaceuticals; Prostate-specific membrane antigen; Nuclear medicine imaging; Radiotherapy; Positron emission tomography/Computed tomography; Preclinical research; Clinical translation and application

1. Introduction

1.1. Prostate cancer and prostate-specific membrane antigen

A primary epithelial malignancy of the prostate, prostate cancer is the predominant cancer affecting the male genitourinary organs. As of 2022, there were approximately

1.5 million new cases of prostate cancer and nearly 400,000 related deaths worldwide. In nearly 60% of countries, prostate cancer is the most prevalent cancer among men. The incidence of prostate cancer also varies geographically, with the highest rates observed in the Caribbean, North America, northern Europe, and Australia, and the lowest rates in Asia and parts of Africa. This disparity is potentially due to differences in prostate cancer screening, diagnosis, and public health interventions between developed and underdeveloped countries.¹ Research findings indicate that the yearly number of newly diagnosed prostate cancers is expected to increase from 1.4 million in 2020 to reach 2.9 million in 2040.² Family history, genetic mutations, and aging are the critical risk factors for prostate cancer, with a few others currently known.³ Malik *et al.*⁴ demonstrated that the incidence of prostate cancer is age-dependent, with the number of cases in men over 80 years old being approximately 40 times higher than that in men under 50 years old. In addition, unhealthy lifestyles, such as smoking and sedentary behavior, as well as dietary habits characterized by high fat, high sugar, high salt, and processed meat consumption, are also potential contributing factors to the development of prostate cancer.⁵

Prostate cancer develops through a multistage

pathological process with distinct pathological changes between early and advanced stages. In early-stage localized prostate cancer, tumorigenesis is mainly driven by overexpression of the androgen receptor (AR) or aberrant activation of its signaling pathway, leading to uncontrolled proliferation of prostatic epithelial cells, reduced apoptosis, and formation of precancerous lesions, while the tumor remains confined within the prostate with low invasiveness.⁶ When AR signaling is strongly suppressed by drugs, tumor cells activate alternative signaling pathways for compensation. Deletion of *PTEN* and sustained activation of the phosphatidylinositol 3-kinase/protein kinase B (PI3K/AKT) growth factor pathway drive tumor progression toward advanced prostate cancer (Figure 1).⁷ As the disease develops to metastatic castration-resistant prostate cancer (mCRPC), sustained activation of AR signaling, complete loss of tumor suppressor function, epithelial–mesenchymal transition, and genome instability collectively enhance cellular invasion, migration, and distant metastasis. Meanwhile, the expression of PSMA is significantly upregulated in advanced lesions.⁸

Prostate-specific membrane antigen is a transmembrane protein of 750 amino acids (aa) found in the central nervous system, comprising a short intracellular domain

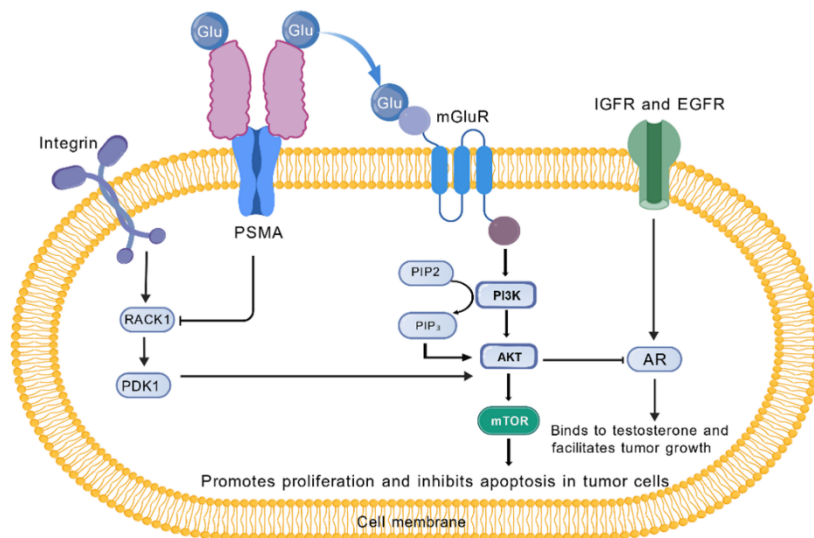


Figure 1. Schematic diagram of prostate-specific membrane antigen (PSMA) and its role in tumorigenesis. Created with BioGDP.com.⁹ Abbreviations: AR: Androgen receptor; EGFR: Epidermal growth factor receptor; Glu: Glutamine; IGFR: Insulin-like growth factor receptor; mGluR: Metabotropic glutamate receptor; mTOR: Mechanistic target of rapamycin; PDK1: 3-Phosphoinositide-dependent protein kinase 1; PI3K: Phosphatidylinositol 3-kinase; PIP₂: Phosphatidylinositol 4,5-bisphosphate; PIP₃: Phosphatidylinositol 3,4,5-trisphosphate; RACK1: Receptor for activated C kinase 1.

(aa 1–19), a transmembrane domain (aa 19–24), and a large, complex extracellular domain (aa 25–750).¹⁰ It exists predominantly as a homodimer on the apical surface of cell membranes, with two catalytic zinc ions in its active site¹¹, and exhibits glutamate carboxypeptidase II activity, catalyzing the hydrolysis of poly- γ -glutamyl groups and N-acetylaspartylglutamate (NAAG). PSMA hydrolyzes NAAG or poly- γ -glutamyl folates to release glutamate, which then binds to metabotropic glutamate receptors (mGluRs) and activates the PI3K/AKT/mechanistic target of rapamycin (mTOR) signaling pathway, enhancing the proliferative and anti-apoptotic capabilities of tumor cells. The upregulation of PSMA promotes the formation of integrin/receptor for activated C kinase 1 (RACK1) complexes and facilitates the conversion of phosphatidylinositol 4,5-bisphosphate (PIP₂) to phosphatidylinositol 3,4,5-trisphosphate (PIP₃), thereby further activating the PI3K/AKT pathway.¹¹ Insulin-like growth factor receptor (IGFR) acts synergistically with epidermal growth factor receptor (EGFR) to activate the AR, resulting in tumorigenesis (Figure 1).

High heterogeneity of PSMA in prostate cancer is an important factor to be considered in its diagnosis and treatment. A study by Jiao *et al.*¹² revealed the effects of differential PSMA expression on the diagnosis of prostate cancer. One of the patients (Figure 2A) presented a maximum standardized uptake value (SUV_{max}) of 2.9 on ⁶⁸Ga-PSMA positron emission tomography/computed tomography (PET/CT) imaging, with negative staining

results (Figure 2B), and was diagnosed with benign prostatic disease. The remaining four patients were confirmed to have prostate cancer. Their Gleason scores were 6 (3 + 3) (Figure 2D), 6 (3 + 3) (Figure 2G), 7 (4 + 3) (Figure 2J), and 8 (4 + 4) (Figure 2M), respectively. All of them showed positive PSMA staining to varying degrees, with the percentage of PSMA-positive cells being 15%, 35%, 57% and 95% in sequence.

Furthermore, castration therapy dynamically regulates PSMA expression. Although some patients show upregulation after androgen deprivation therapy (ADT), long-term ADT may have the opposite effect—reducing expression, particularly in those with castration-sensitive prostate cancer. This reduction markedly impairs radioligand therapy tracer uptake.¹³ Pabst *et al.*¹⁴ reported low or negative PSMA uptake on PET scans in patients treated with first-line chemotherapy and ADT. Preclinical studies have verified that short-term ADT can markedly upregulate PSMA expression at the cellular and animal model levels, thereby increasing the uptake of PSMA-targeted tracers.¹⁵ Nevertheless, a retrospective study clearly demonstrated that long-term ADT significantly reduces the detectability of hormone-sensitive prostate cancer on PSMA PET/CT.¹⁶

During treatment, some tumor lesions undergo transdifferentiation into neuroendocrine prostate cancer (NEPC), a highly aggressive subtype with an extremely poor prognosis characterized by the loss of biomarkers,

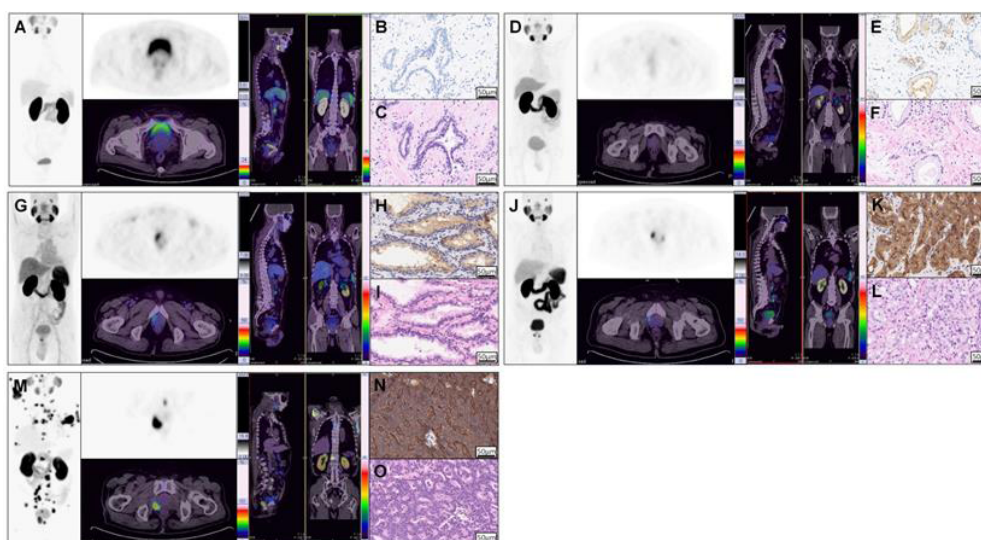


Figure 2. Representative ⁶⁸Ga-prostate-specific membrane antigen (PSMA) positron emission tomography/computed tomography (PET/CT) images, along with corresponding immunohistochemical (IHC) and hematoxylin-eosin (HE) staining results, demonstrate a strong correlation between maximum standardized uptake value (SUV_{max}) and PSMA expression in prostate tissues. (A, D, G, J, M) PET/CT images. (B, E, H, K, N) PSMA staining. (C, F, I, L, O) HE staining for one subject with benign prostatic disease (A–C) and four individuals with prostate cancer (D–O). Reprinted from Jiao *et al.*¹²

including AR and PSMA.¹⁷ Significant downregulation of *FOLH1*, the gene encoding PSMA, has been observed in specimens from NEPC patients and adenocarcinoma samples with neuroendocrine gene expression signatures.^{18,19} Tumor cells transformed into NEPC not only lose dependence on AR signaling but also generally exhibit concurrent downregulation of AR, prostate-specific antigen, and PSMA.²⁰ An immunohistochemical study revealed prominent histological and biomarker expression differences between prostate cancer and NEPC. Histomorphology was assessed via hematoxylin-eosin (HE) staining, combined with immunohistochemical staining for PSA and synaptophysin (SYP). Prostatic adenocarcinoma tissues highly expressed PSA but not SYP, showing typical luminal epithelial differentiation (Figure 3). In contrast, NEPC tissues presented strong positive SYP staining with absent or barely detectable PSA expression, indicating a neuroendocrine differentiation phenotype.¹⁷ Such transdifferentiation leads to resistance to standard therapies, including ADT targeting AR signaling. Accordingly, patients with PSMA-negative NEPC can barely benefit from conventional PSMA-targeted therapy.

1.2. Radiopharmaceuticals and positron emission tomography/computed tomography

In 1898, the Curies discovered the new radioactive elements polonium and radium.²¹ In 1936, John H. Lawrence used ³²P to treat leukemia for the first time. In 1941, Saul Hertz applied radioactive ¹³¹I to thyroid disease treatment, marking the beginning of the development

of radiopharmaceuticals.²² Radiopharmaceuticals are a special class of drugs composed of radioactive nuclides, chelating agents, linkers, and targeted ligands, where ligands are antibodies, peptides, or small-molecule drugs. Radionuclides are divided into diagnostic (^{99m}Tc, ¹¹¹In, ¹²³I, ¹⁸F) and therapeutic (¹³¹I, ⁹⁰Y, ¹⁷⁷Lu, ²²⁵Ac) types. When conjugated with targeted ligands, these radionuclides enable both visualized diagnosis and precise targeted therapy of diseases²³ (Figure 4).

Traditional clinical confirmatory methods for prostate cancer include PSA testing, digital rectal examination, transrectal ultrasound, magnetic resonance imaging, and prostate needle biopsy. In recent years, PET/CT has emerged as a tool to detect prostate cancer and distinguish it from benign lesions.²⁴ It combines functional metabolic imaging (PET) with anatomical imaging (CT). Similar to PET/CT, single-photon emission computed tomography (SPECT)/CT is another hybrid technique that integrates radionuclide imaging with anatomical imaging. By detecting single gamma photons emitted from intravenously administered tracers (e.g., ^{99m}Tc, ¹²³I, ¹⁷⁷Lu), SPECT/CT provides molecular functional information on metabolism, blood perfusion, and receptor expression in organs or lesions. Combined with CT's high-resolution anatomical images, it enables precise localization. Although SPECT/CT has lower equipment and tracer costs than PET/CT, its spatial resolution and quantitative performance are inferior.²⁵

The radiotracers of PET/CT are typically formed by

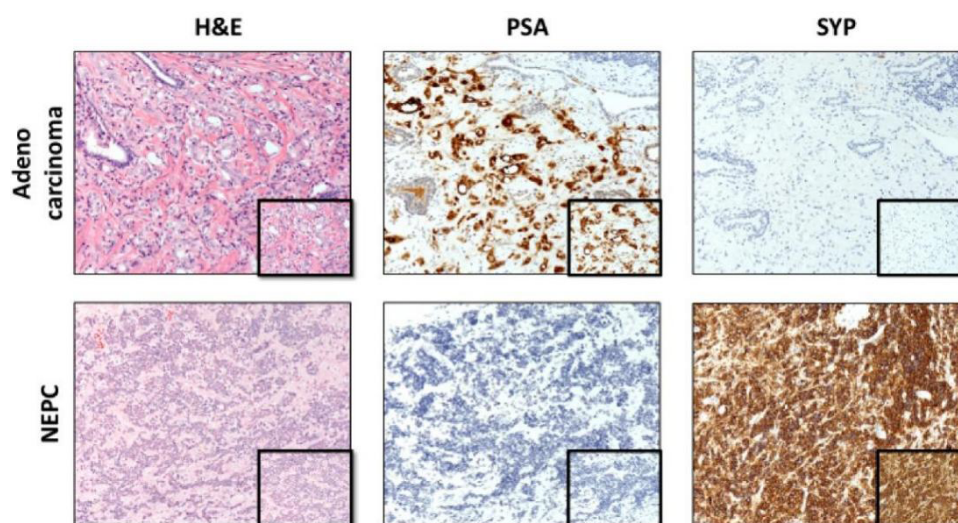


Figure 3. Immunohistochemical evaluation of prostate adenocarcinoma and neuroendocrine prostate cancer (NEPC). Reprinted from Maylin *et al.*¹⁷ Abbreviations: H & E: Hematoxylin and eosin; PSA: Prostate-specific antigen; SYP: Synaptophysin.

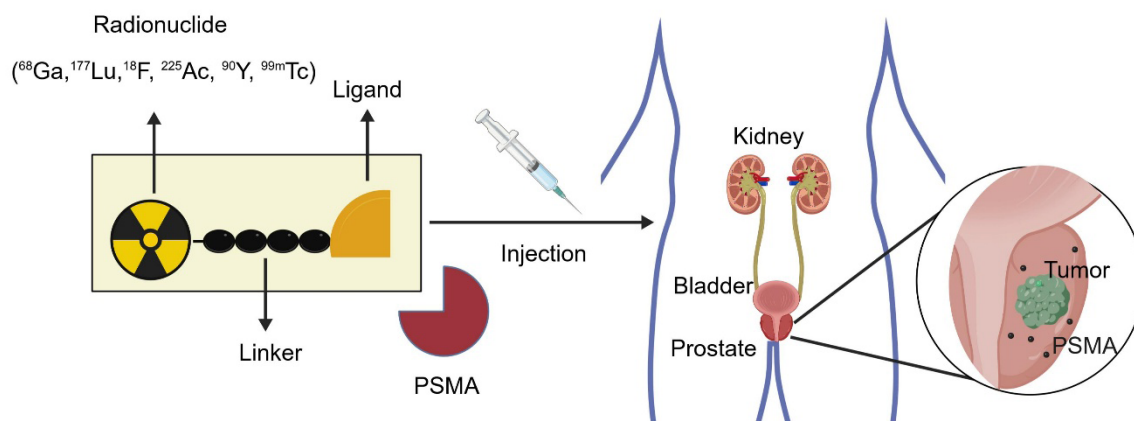


Figure 4. The workflow of prostate-specific membrane antigen (PSMA)-targeted radiopharmaceuticals for the diagnosis and treatment of prostate cancer. Created with BioGDP.com.⁹

conjugating positron-emitting radionuclides with targeted ligands. The most common radiotracer is fluorine-18 fluorodeoxyglucose (FDG). Leveraging the targeting capability of FDG and the positron-emission property of ^{18}F , FDG-PET/CT precisely localizes primary and metastatic prostate cancer lesions by detecting tumor cell metabolic activity.²⁶ Based on the principle that tumor cells exhibit high metabolism and massive glucose uptake, this technique detects ^{18}F -FDG accumulation to reveal lesion location and extent, simultaneously providing both functional metabolic information and anatomical localization. As a result, it is widely used for tumor staging, therapeutic effect evaluation, and recurrence monitoring.^{27,28}

Compared with classical diagnostic methods for prostate cancer, PET/CT has ultra-high sensitivity and specificity for tumor cells, enables integrated whole-body scanning, and allows assessment of both primary and metastatic lesions.^{28,29} However, ^{18}F -FDG has significant limitations. As a non-specific tumor radiotracer, it can produce false-positive results in various non-cancerous conditions, including inflammatory infections³⁰, benign tumors such as pituitary adenomas³¹, and adrenal tumors.³² Tumors with high expression of membrane glucose transporters and hexokinase typically show high ^{18}F -FDG uptake.³³ In contrast, hypometabolic tumors, such as well-differentiated hepatocellular carcinoma³⁴ and prostate cancer, may yield false-negative results, leading to missed diagnoses. Additionally, the use of oral hypoglycemic agents or insulin can further alter ^{18}F -FDG biodistribution.³⁵

Taking advantage of PSMA's differential expression between prostate cancer cells and normal tissue¹⁰, PSMA-PET/CT is a common and effective diagnostic method for prostate cancer, demonstrating a higher detection rate than FDG-PET/CT.³⁶ This differential expression also establishes PSMA as an important biomarker and drug target for both diagnosis and treatment.^{37,38} Nowadays, several breakthrough achievements have been made in the development of PSMA-targeted radiopharmaceuticals. In December 2020, ^{68}Ga -PSMA-11 was approved by the United States Food and Drug Administration (FDA) as a PET imaging tracer for the diagnosis of metastatic or recurrent prostate cancer.^{39,40} ^{177}Lu -PSMA-617 was then approved by the FDA in March 2022 for targeted radioligand therapy in patients with PSMA-positive mCRPC.⁴¹ Currently, ^{225}Ac -PSMA-617 is undergoing clinical trials for targeted alpha-particle therapy of mCRPC.^{42,43} Beyond its prevalence in prostate cancer, PSMA exhibits low-level expression in normal tissues, including the kidneys, salivary glands, and gastrointestinal tract, leading to off-target uptake of PSMA-based radioligands and complicating their development.^{44,45} To enhance tumor targeting, prolong retention in tumor cells, reduce off-target organ uptake, and minimize incorrect and undetected diagnoses caused by PSMA heterogeneity, researchers have developed a series of dual-target drugs with both radiodiagnostic and therapeutic functions based on PSMA monovalent ligands through appropriate structural modifications, introduction of plasma albumin-binding moieties⁴⁶, modification of chelator types, and combination with pan-cancer targets.⁴⁷ This review focuses

on single-target small-molecule inhibitors of PSMA and PSMA-based heterodimers with other pan-cancer targets.

2. Prostate-specific membrane antigen molecule inhibitors

As a peptide neurotransmitter, NAAG is broadly present across the mammalian nervous system. Both in vitro and in vivo, NAAG is specifically hydrolyzed by PSMA to release N-acetylaspartate and glutamate. Researchers have used NAAG as a lead compound to design analogs that specifically bind to PSMA.⁴⁷ Through structural modification and optimization of NAAG, a pharmacophore for PSMA inhibitors is generated, featuring a basic structure composed of glutamate and lysine connected by a urea group.

2.1. Monovalent ligands

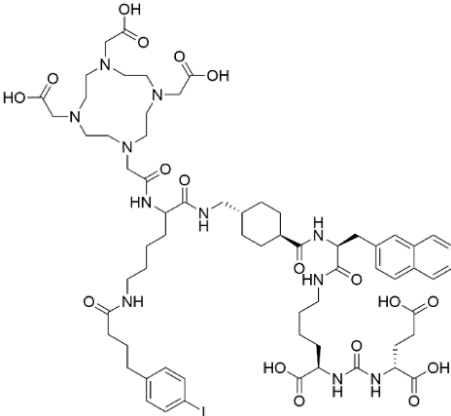
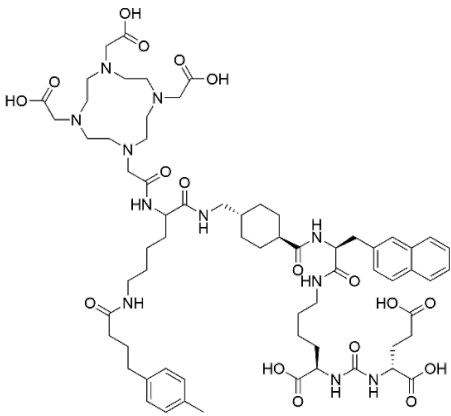
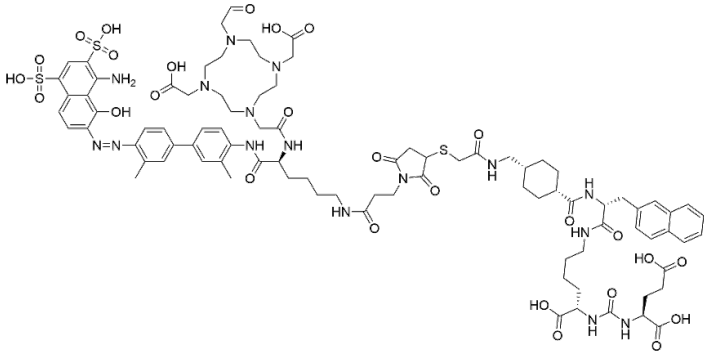
In 2012, Eder *et al.*⁴⁰ reported the progress of two small-molecule PSMA-specific inhibitors: PSMA-11 (number 1 in Table 1) and Glu-Urea-Lys (Ahx)-1,4,7,10-tetraazacyclododecane-1,4,7,10-tetraacetic acid (DOTA). Using Lys-Urea-Glu as the basic structural unit, they attached 6-aminocaproic acid to the lysine residue, which was subsequently conjugated with the open-chain chelator N,N'-bis[2-hydroxy-5-(carboxyethyl) benzyl] ethylenediamine-N,N'-diacetic acid (HBED-CC) and the macrocyclic chelator DOTA. In vivo distribution studies in tumor-bearing mouse models revealed that ⁶⁸Ga-labeled PSMA-11 exhibited optimal targeting performance. One hour after injection, the LNCaP tumors' uptake reached $7.70 \pm 1.45\%$ injected dose (ID)/g, which was significantly

Table 1. Chemical structures of representative prostate-specific membrane antigen (PSMA) ligands

Number	Ligand	Chemical structure	Reference
1	PSMA-11		40
2	PSMA-617		48
3	PSMA-I&T		49

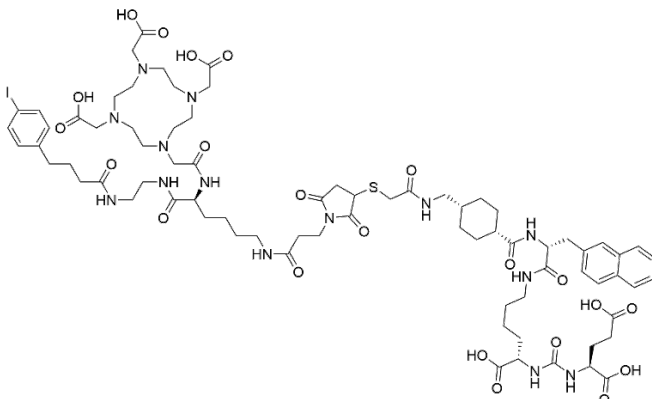
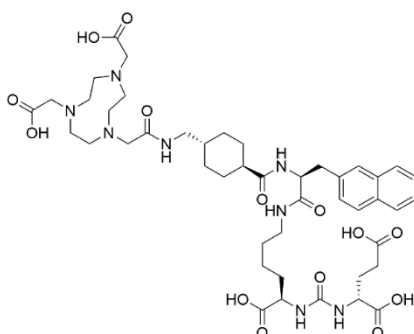
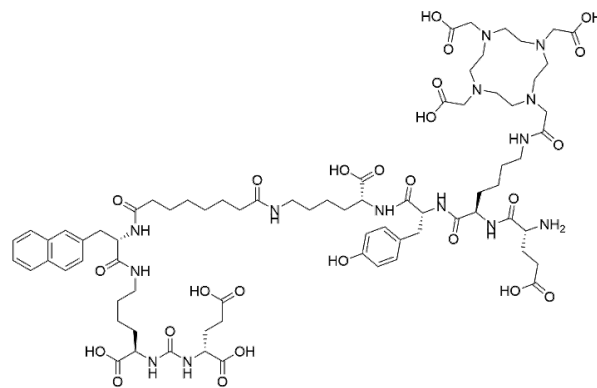
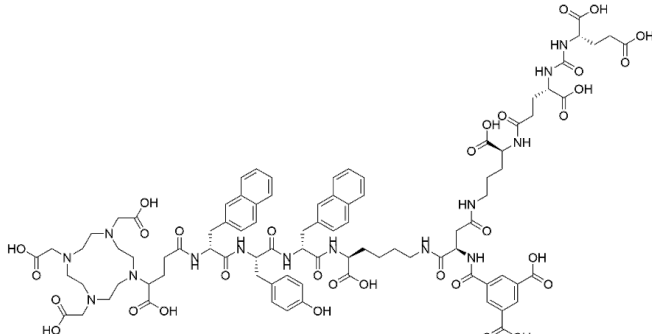
(Cont'd...)

Table 1. (Continued)

Number	Ligand	Chemical structure	Reference
4	PSMA-ALB-53		50
5	PSMA-ALB-56		50
6	EB-PSMA-617		51

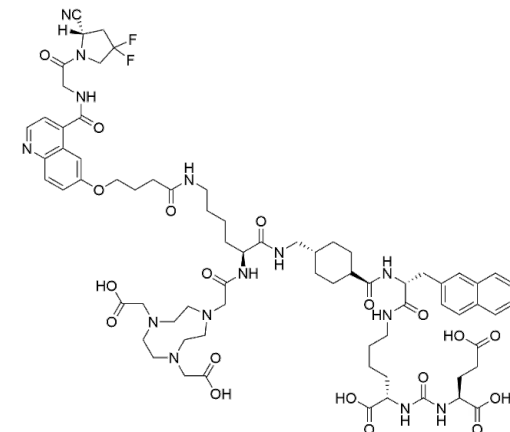
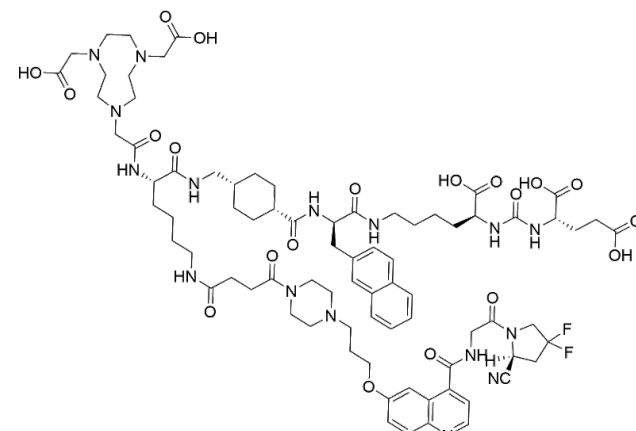
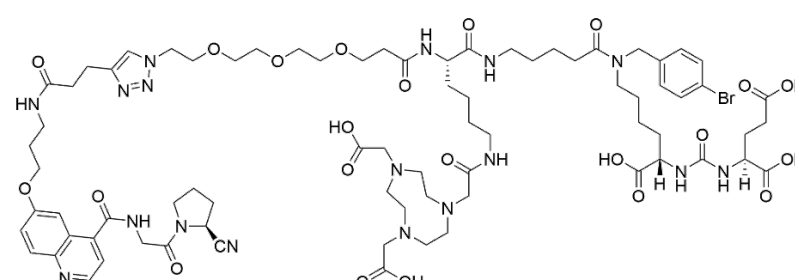
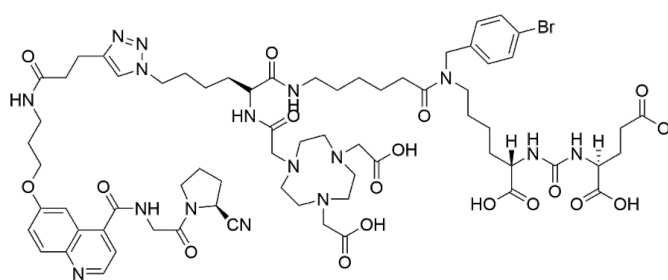
(Cont'd...)

Table 1. (Continued)

Number	Ligand	Chemical structure	Reference
7	IP-PSMA-617		51
8	PSMA-BCH		52
9	NYM-032		53
10	PSMA-TO-1		54

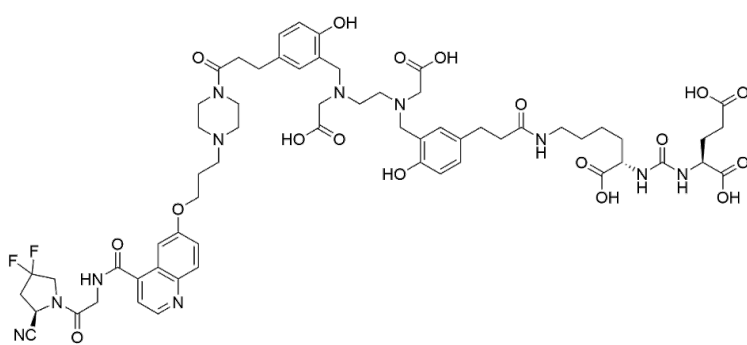
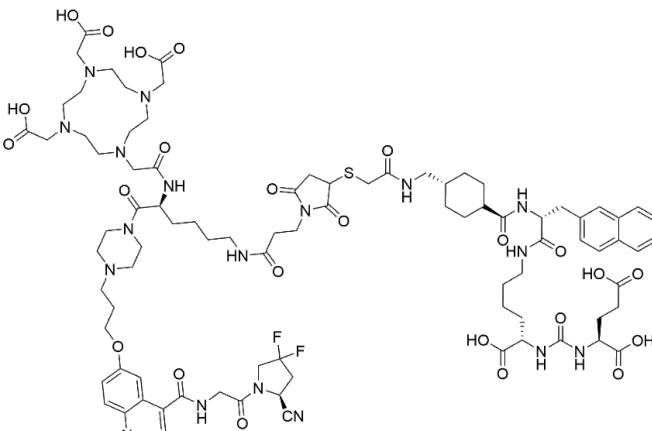
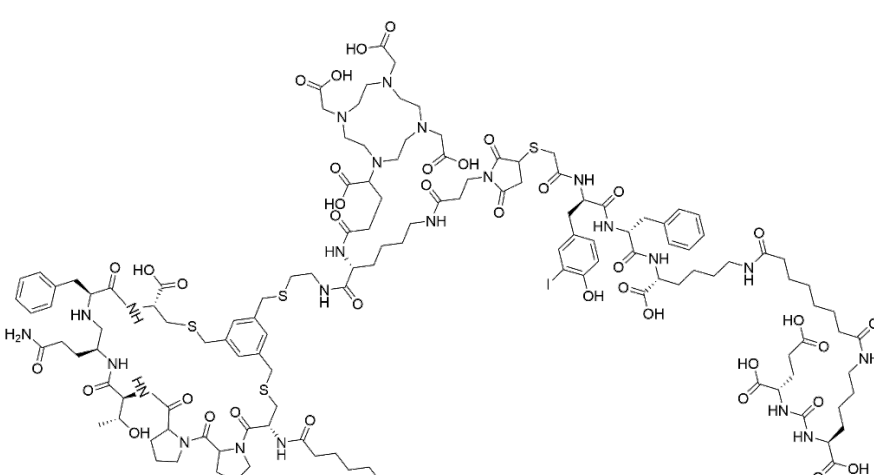
(Cont'd...)

Table 1. (Continued)

Number	Ligand	Chemical structure	Reference
11	NOTA-PSMA-FAPI-01		55
12	NOTA-PSMA-FAPI-02		55
13	FP-L1		56
14	FP-L2		56

(Cont'd...)

Table 1. (Continued)

Number	Ligand	Chemical structure	Reference
15	PSEA-01		57
16	FAPI-PSMA		58
17	PSMA-FAPI-01		59

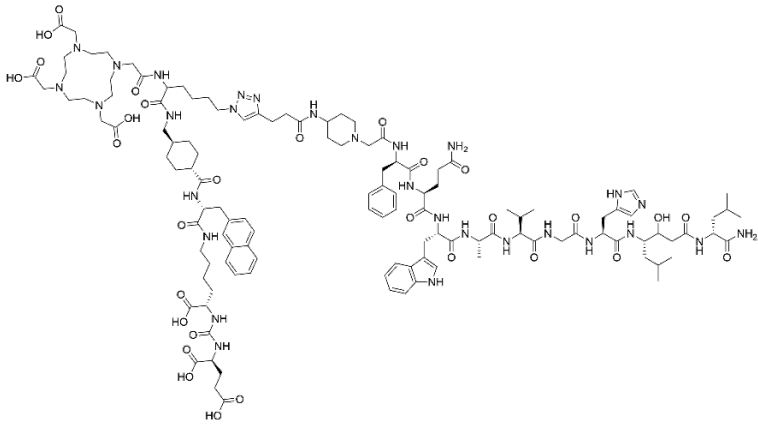
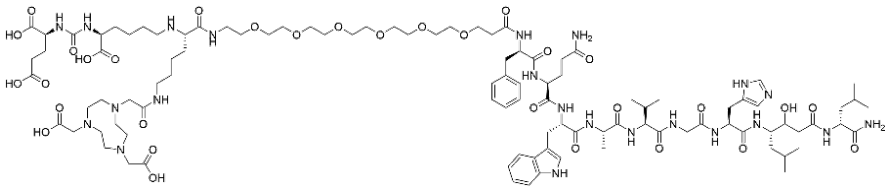
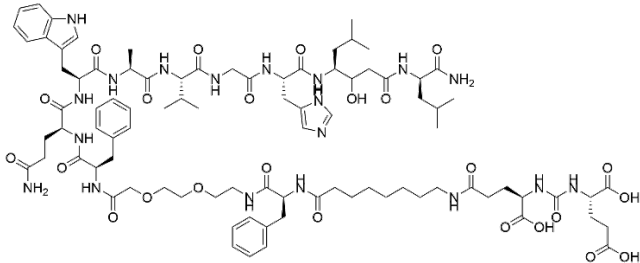
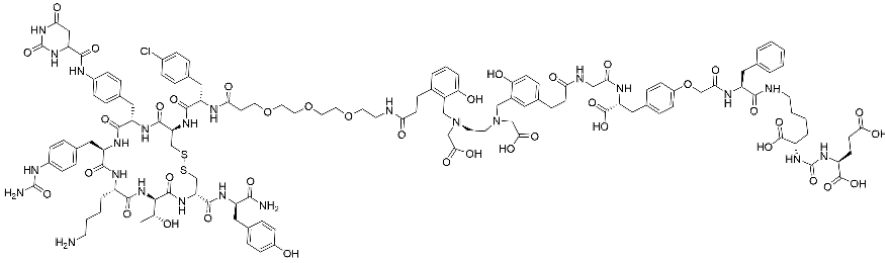
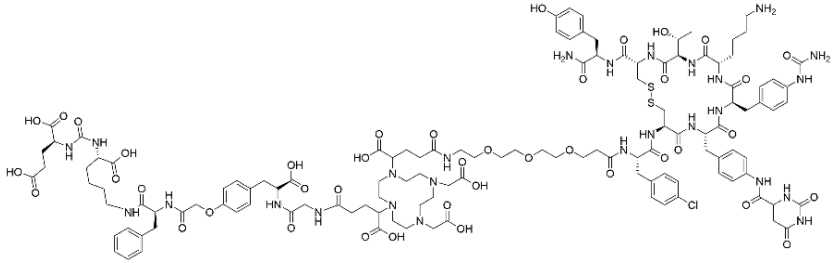
(Cont'd...)

Table 1. (Continued)

Number	Ligand	Chemical structure	Reference
18	PSMA-FAPI-02		59
19	[^{99m} Tc]-HGFAPI		60
20	[^{99m} Tc]Tc-HPSMA		60
21	[^{99m} Tc]Tc-HFaPSMA		60

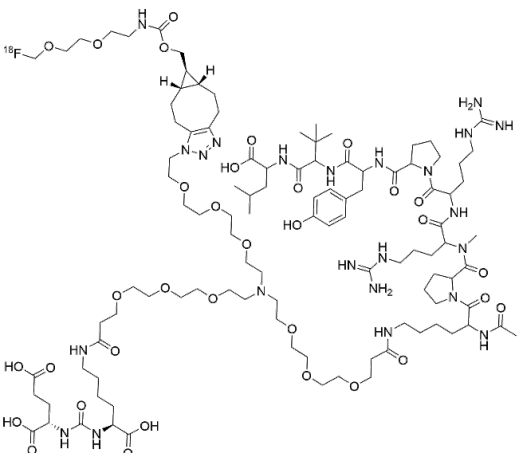
(Cont'd...)

Table 1. (Continued)

Number	Ligand	Chemical structure	Reference
22	RM2-PSMA-617		61
23	NOTA-DUPA-RM26		62
24	BQ7812		63
25	PSMA-SSTR2-1		64
26	PSMA-SSTR2-2		64

(Cont'd...)

Table 1. (Continued)

Number	Ligand	Chemical structure	Reference
27	[¹⁸ F]F-BCN-PSMA-NT		65

greater than that of DOTA-based contrast agents ($2.97 \pm 0.48\%ID/g$). The aromatic structure of HBED-CC produces favorable interactions with the hydrophobic pocket of PSMA, thereby improving the targeting specificity, internalization efficiency, and tumor imaging quality of the probe. To further enhance the specific targeting capability of PSMA-11, Schäfer M *et al.*⁶⁶ designed and synthesized a dimerized PSMA-11 ligand. This molecule was constructed by coupling two PSMA-11 moieties via an HBED-CC chelator.

The acyclic chelator HBED-CC of PSMA-11 fits well for ⁶⁸Ga labeling but is incompatible with ¹⁷⁷Lu. To bridge the gap toward prostate cancer theranostics, Benešová *et al.*⁴⁸ developed PSMA-617 (number 2 in Table 1) in 2015, a novel inhibitor featuring an optimized linker designed to accommodate both diagnostic and therapeutic radionuclides. The molecule mainly consists of three moieties: the pharmacophore Lys-Urea-Glu, the chelator DOTA, and an optimized linker. Weineisen *et al.*⁴⁹ designed PSMA-I&T (number 3 in Table 1), a theranostic probe applicable for both diagnostic and therapeutic applications. In contrast to the naphthyl linker in PSMA-617, PSMA-I&T utilizes a linker containing the Lys-Phe-Phe peptide unit (Figure 5), which enhances its binding affinity to PSMA by strengthening hydrophobic interactions between the probe and PSMA.

Using mice bearing PC295 PDX tumors, SPECT/CT imaging (Figure 4A,C) showed that both [¹⁷⁷Lu]Lu-PSMA-617 and [¹⁷⁷Lu]Lu-PSMA-I&T clearly target xenograft tumors after injection. However, [¹⁷⁷Lu]Lu-PSMA-I&T performed improved and more prolonged radioactivity retention in the bladder and kidneys,

demonstrating that it is predominantly metabolized via urinary excretion. Quantitative biodistribution analysis (Figure 5B,D) showed that the tumor uptake of [¹⁷⁷Lu]Lu-PSMA-617 was 6–8 %IA/g at 4 h after injection, slightly decreased at 8 h, and declined to 3–4 %IA/g at 24 h. The tumor uptake of [¹⁷⁷Lu]Lu-PSMA-I&T was comparable to (or even slightly higher than) that of [¹⁷⁷Lu]Lu-PSMA-617. Nevertheless, its renal uptake reached 13–20 %IA/g at 4 h and 8 h, which was 30-fold higher than that of [¹⁷⁷Lu]Lu-PSMA-617, leading to a markedly inferior tumor-to-kidney ratio at all time points. Although both tracers possessed comparable tumor-targeting capability, the prominently elevated renal retention of [¹⁷⁷Lu]Lu-PSMA-I&T suggests an increased risk of renal radiation dose. In contrast, [¹⁷⁷Lu]Lu-PSMA-617 presents a beneficial tumor-kidney dose distribution and serves as a safer therapeutic candidate.⁶⁷

Gühne *et al.*⁶⁸ conducted a clinical study in which three patients were injected with [⁶⁸Ga]Ga-PSMA-11, [⁶⁸Ga]Ga-PSMA-617, and [⁶⁸Ga]Ga-PSMA-I&T, respectively. All three radiotracers exhibited physiological high uptake in salivary glands, spleen, duodenum, and kidneys, and a distinct recurrent tumor lesion was detected in the pelvic region of each patient. The hepatic uptake of [⁶⁸Ga]Ga-PSMA-11 was markedly superior to that of the other two tracers, while its bone uptake was lower than that of PSMA-617. Quantitative analysis further verified that the accumulation in normal organs, including blood, muscle, and bone, showed a significant decreasing trend in the order of PSMA-617 > PSMA-I&T > PSMA-11 (Figure 6). In key clinical scenarios, the three [⁶⁸Ga]Ga-PSMA ligands present equivalent applicability.

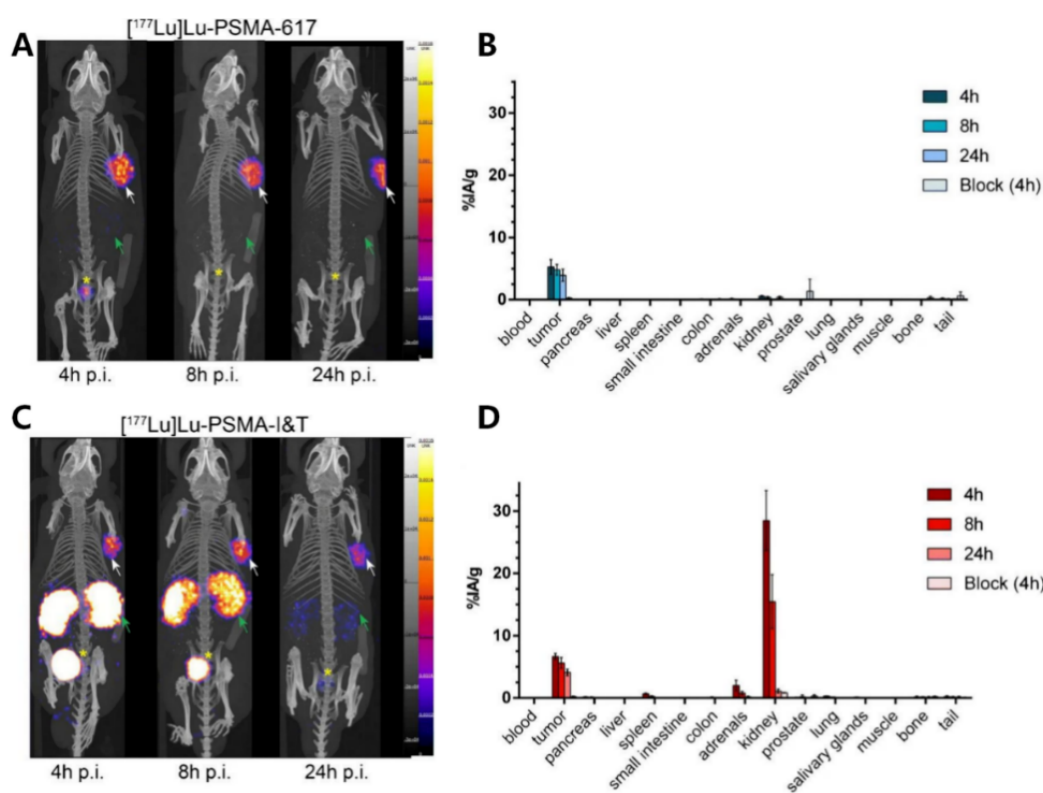


Figure 5. Autoradiography (ex vivo and in vitro) of PC295 patient-derived xenograft (PDX) models and murine renal tissues. (A) Typical single-photon emission computed tomography (SPECT) scans acquired at 4, 8, and 24 h post-injection of $[^{177}\text{Lu}]\text{Lu-PSMA-617}$. The PC295 PDX is marked with white arrows, the kidneys with green arrows, and the bladder with yellow asterisks. (B) Biodistribution data for $[^{177}\text{Lu}]\text{Lu-PSMA-617}$, given as percent of injected activity per gram of tissue (%IA/g). (C) Representative SPECT scans obtained at 4, 8, and 24 h after administration of $[^{177}\text{Lu}]\text{Lu-PSMA-I\&T}$. White arrows point to the PC295 PDX, green arrows to the kidneys, and yellow asterisks to the urinary bladder. (D) Biodistribution data for $[^{177}\text{Lu}]\text{Lu-PSMA-I\&T}$, presented as %IA/g. Modified from Ruigrok *et al.*⁶⁷

The most frequently utilized albumin binders to date are 4-(p-iodophenyl)butyric acid and truncated Evans blue fragments.^{69,70} Lau *et al.*⁶⁹ revealed that conjugating albumin binders to radioligands significantly prolongs the blood circulation time of tracers and improves therapeutic efficacy. Umbricht *et al.*⁵⁰ and Benešová *et al.*⁷¹ designed and synthesized PSMA-ALB-53 (number 4 in Table 1; containing a strong albumin-binding 4-iodophenyl group) and PSMA-ALB-56 (number 5 in Table 1; containing a weak albumin-binding p-tolyl group). The tumor uptake of $[^{177}\text{Lu}]\text{Lu-PSMA-ALB-53}$ in PC3-PIP lesions increased continuously over the first two days. $[^{177}\text{Lu}]\text{Lu-PSMA-ALB-56}$ exhibited notable tumor accumulation as early as 24 h post-injection and accelerated renal elimination, with renal uptake rapidly reaching $45.9 \pm 11.3\%$ injected activity (IA)/g within 1 h. Both tracers showed continuously lower radioactive uptake in PC3 flu tumors compared to blood over the whole observation time (Figure 7).^{50,71}

Maximum-intensity-projection SPECT images of $[^{177}\text{Lu}]$

Lu-PSMA-ALB-56 in patients with mCRPC revealed that, from 1.5 h to 7 days after injection, the radiotracer mainly accumulated in the parotid glands, kidneys, lacrimal glands, submandibular glands, and the blood pool. Tumor lesion uptake increased gradually over time, showed the highest contrast at 48 h, and remained visible for up to 7 days. Radioactivity in the red bone marrow and blood declined rapidly, with values of 0.0161%IA/g at 5 min, dropping to 0.0052%IA/g at 6 h, and decreasing to only 0.0004%IA/g at 7 days. Renal uptake peaked at 24 h (0.023%IA/g). The parotid and submandibular glands also reached their maximum uptake at 24 h, at 0.0107%IA/g and 0.0093%IA/g, respectively. Notably, tumor uptake rose continuously and reached 0.134%IA/g at 48 h, reflecting high tumor accumulation resulting from the prolonged circulation time of albumin-binding ligands. The eyes had an early uptake peak (within 6 h) that cleared rapidly, while the liver and spleen maintained low radioactivity for the whole observation period (Figure 8).⁷²

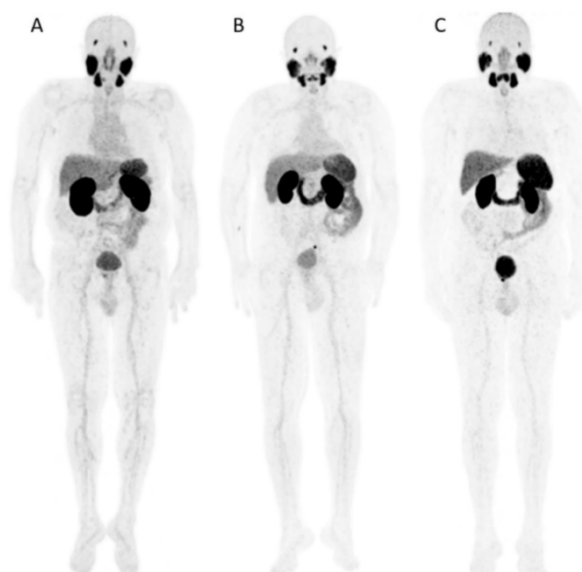


Figure 6. Representative patients administered with ^{68}Ga PSMA-617 (A), ^{68}Ga PSMA-I&T (B), and ^{68}Ga PSMA-11 (C) are shown. Positron emission tomography maximum-intensity projection images reveal pronounced radiotracer accumulation in the kidneys, salivary glands, spleen, and duodenum—a common feature among the three agents. In each patient, a solitary pelvic recurrence focus is visible adjacent to the urinary bladder, albeit with varying uptake intensities. Notably, the blood-pool activity differs visibly among the tracers, with ^{68}Ga PSMA-11 showing the lowest retention (C). Reprinted from Gühne *et al.*⁶⁸

Wang *et al.*⁵¹ developed two PSMA-targeted ligands conjugated with albumin binders: EB-PSMA-617 and IP-PSMA-617 (numbers 6 and 7, respectively, in Table 1). Representative coronal PET images of ^{86}Y -labeled EB-PSMA-617, IP-PSMA-617, and PSMA-617 in PC-3 PIP (PSMA⁺) tumor-bearing mice revealed that, unlike rapidly cleared ^{86}Y -PSMA-617, both albumin-binding ligands exhibited high tumor uptake from 4 h to 48 h. Overall, owing to slower blood clearance and a unique cellular retention mechanism, EB-PSMA-617 achieved higher tumor uptake at a lower administered dose compared with PSMA-617 (Figure 9).

Liu *et al.*⁵² developed an ^{18}F -labeled, 1,4,7-triazacyclononane-1,4,7-triacetic acid (NOTA)-conjugated PSMA-targeted ligand, PSMA-BCH (number 8 in Table 1). Compared with ^{68}Ga (half-life: 68 min), ^{18}F has a longer half-life (110 min) and lower positron energy. The decreased energy results in a briefer tissue penetration range of ^{18}F , which theoretically enables higher imaging resolution, facilitating precise lesion localization and improving the detection of small lesions. ^{18}F AlF-PSMA-BCH features rapid and straightforward preparation (one-step labeling within 30 mins, with a 32.2% radiochemical yield and >99% radiochemical purity), favorable physicochemical properties (hydrophilicity and highly stable in vivo and in vitro), high PSMA binding affinity

($K_d = 2.90$ nM), and excellent specificity (tumor uptake of 7.87%ID/g). The tumor-to-muscle ratio of this tracer in tumor-bearing mice reached 64.5, outperforming ^{68}Ga Ga-PSMA-617.

Fu *et al.*⁵³ replaced the cyclohexane moiety of PSMA-617 with long-chain fatty acids and introduced *D*-tyrosine and *D*-lysine to develop NYM-032 (number 9 in Table 1). Preclinical and preliminary clinical studies demonstrated that ^{68}Ga NYM-032 presented substantially superior SUV_{max} in bone and lymph node metastases than PSMA-617, with favorable safety profiles. In LNCaP xenografts, ^{177}Lu NYM-032 showed sustained tumor retention, achieving a tumor uptake of 17.16%ID/g at 120 h post-injection. A single high dose of 74 MBq markedly inhibits tumor growth.

In a preclinical study conducted by Meyer *et al.*⁵⁴, the performance of the novel PSMA ligand PSMA-TO-1 (number 10 in Table 1) was compared with the conventional ligands PSMA-617 and PSMA-11. Preclinical PET imaging showed that ^{68}Ga PSMA-617 exhibited the highest tumor uptake (mean: 15.46%IA/g), followed by PSMA-TO-1 (11.27%IA/g). Biodistribution comparison between ^{177}Lu PSMA-TO-1 and ^{177}Lu PSMA-617 revealed that, although PSMA-617 showed slightly higher tumor retention at 1 h ($14.4 \pm 10.2\%$ IA/g vs. 10.2%IA/g), PSMA-TO-1 exhibited higher tumor accumulation at

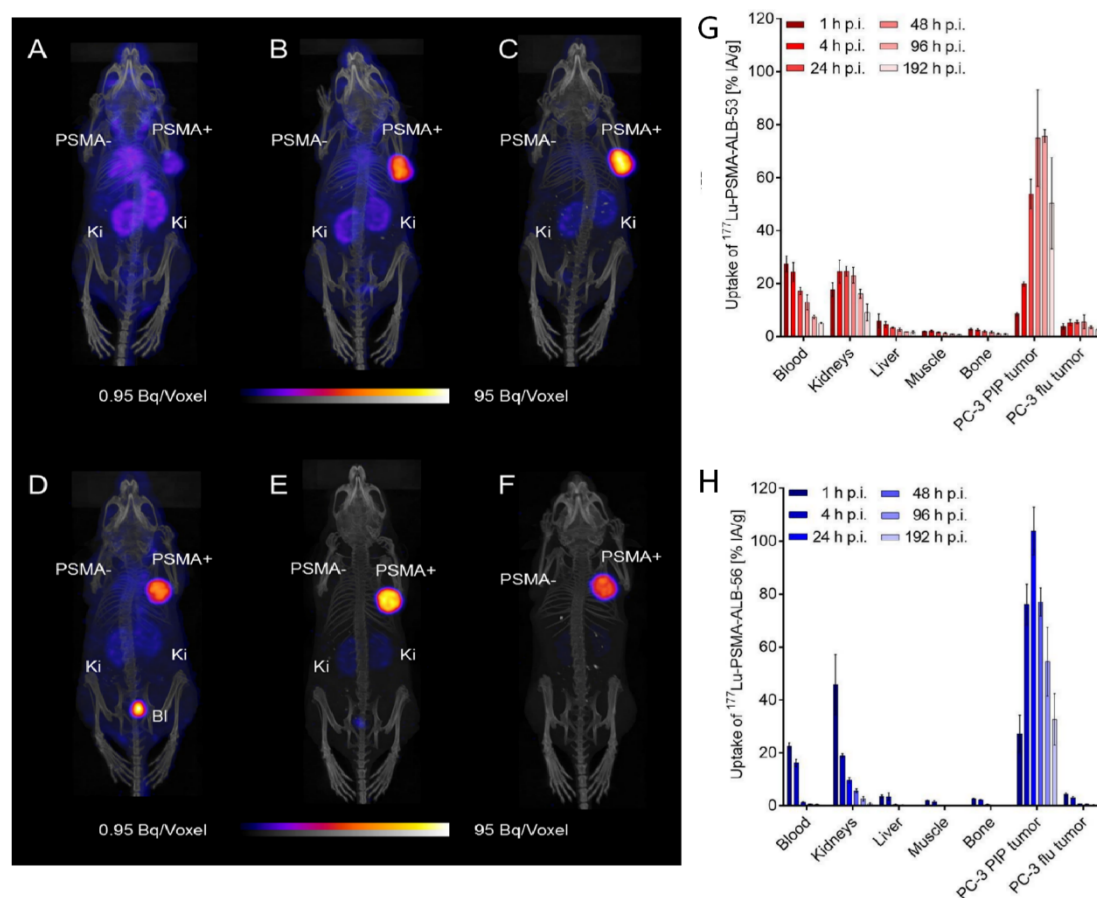


Figure 7. Single-photon emission computed tomography/computed tomography (SPECT/CT) images displayed as maximum intensity projections (MIPs) of PC-3-PIP/flu tumor-bearing mice at various time points following injection of $[^{177}\text{Lu}]\text{Lu-PSMA-ALB-53}$ and $[^{177}\text{Lu}]\text{Lu-PSMA-ALB-56}$ (A–C). MIPs of a mouse at 4 h (A), 24 h (B), and 72 h (C) after administration of $[^{177}\text{Lu}]\text{Lu-PSMA-ALB-53}$ (25 MBq, 1 nmol). (D–F) MIPs of a mouse at 4 h (D), 24 h (E), and 72 h (F) after injection of $[^{177}\text{Lu}]\text{Lu-PSMA-ALB-56}$ (25 MBq, 1 nmol). (G) and (H) Biodistribution profiles of the radioligands obtained in Balb/c nude mice bearing PC-3 PIP and PC-3 flu tumor xenografts on the right and left shoulder, respectively. Time-dependent tissue distribution of $[^{177}\text{Lu}]\text{Lu-PSMA-ALB-53}$ (5 MBq, 1 nmol) (G) and $[^{177}\text{Lu}]\text{Lu-PSMA-ALB-56}$ (5 MBq, 1 nmol) (H). Data are presented as mean \pm SD ($n = 3\text{--}6$ mice per time point). Reprinted with permission from Umbricht CA *et al.*⁵⁰ Copyright © 2018 American Chemical Society. Abbreviations: Bl: Urinary bladder; Ki: Kidney; PSMA: Prostate-specific membrane antigen; PSMA⁺: PSMA-positive PC-3 PIP tumor; PSMA⁻: PSMA-negative PC-3 flu tumor.

all subsequent time points. Nevertheless, PSMA-TO-1 presented prominently elevated renal uptake, reaching 24%IA/g at 24 h (Figure 10).

2.2. Bivalent ligands

Heterogeneity of PSMA expression in prostate cancer cells reduces the radiation dose delivered by PSMA-targeting ligands. Tackling the challenges posed by tumor heterogeneity is essential for enhancing the diagnosis and prognosis of advanced prostate cancer. The research strategy of “a single molecule targeting multiple receptors” can be referenced to design the functionality of bispecific radiotracers. Existing studies have shown that bivalent

molecular ligands—obtained by covalently linking two molecules targeting different receptors—are able to significantly optimize the pharmacokinetic properties of monovalent ligands, enhance tumor accumulation, increase imaging contrast, and reduce non-target uptake.⁵⁹

2.2.1. Prostate-specific membrane antigen–fibroblast activation protein heterodimer

Fibroblast activation protein (FAP) belongs to the class of type II transmembrane proteins consisting of 760 amino acids. It is barely expressed in normal tissues but is upregulated in cancer-associated fibroblasts within the peritumoral environment of various carcinomas. FAP

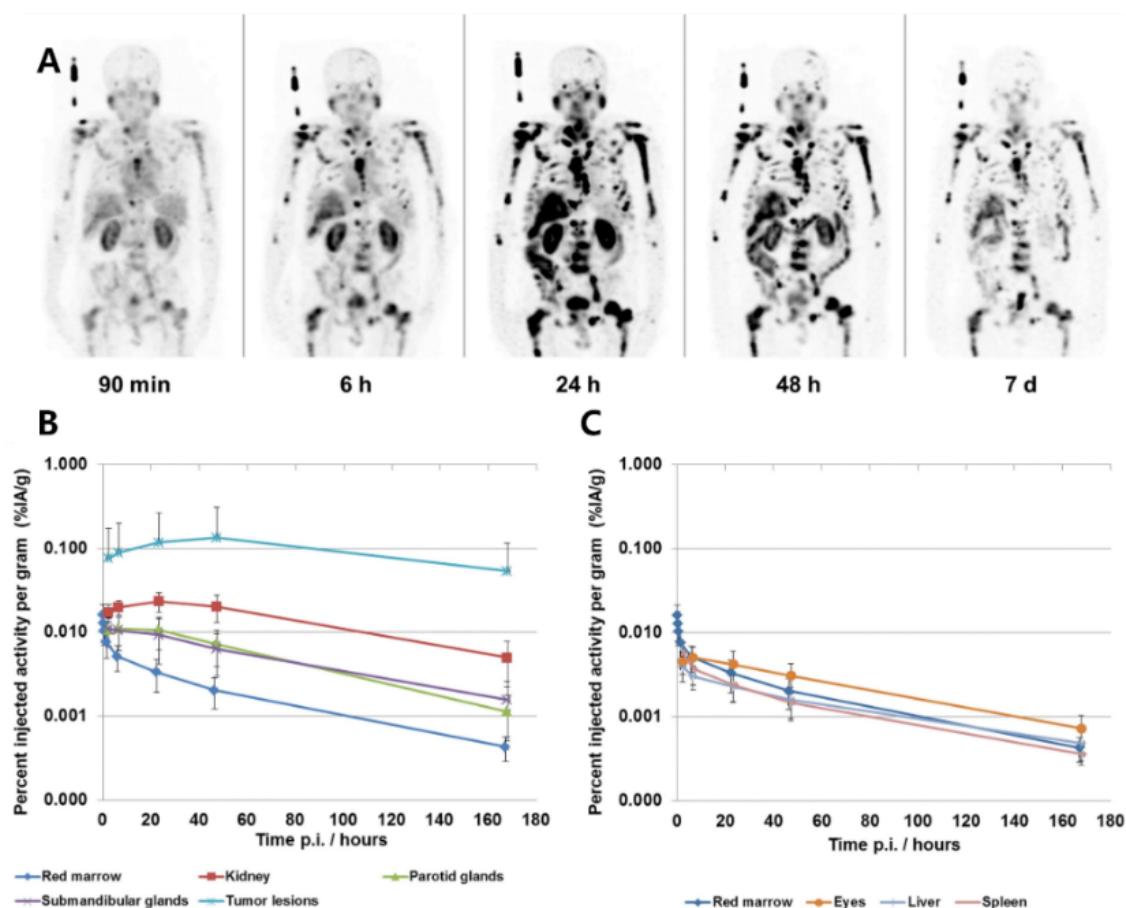


Figure 8. Single-photon emission computed tomography (SPECT) imaging of $[^{177}\text{Lu}]\text{Lu-PSMA-ALB-56}$ and time-activity curves (TACs) for various organs, tissues, and lesions. (A) SPECT maximum-intensity projection images of $[^{177}\text{Lu}]\text{Lu-PSMA-ALB-56}$. (B) TACs for red marrow, kidneys, parotid glands, submandibular glands, and tumor lesions, presented as percent injected activity per gram of tissue (%IA/g). (C) TACs for red marrow, eyes, liver, and spleen, expressed as %IA/g. Reprinted from Kramer *et al.*⁷²

exerts its functions at the cell surface, acting on diverse hormones and extracellular matrix components, and is involved in processes such as tissue remodeling, fibrosis, wound repair, inflammation, and cancer development.⁴⁷ As a protease, FAP enhances the invasiveness of tumor cells into the extracellular matrix and promotes tumor growth and proliferation. Given that PSMA and FAP are co-present in a range of cancers, including prostate cancer, colorectal cancer, lung cancer, pancreatic cancer, gastric cancer, and thyroid cancer, the design and development of heterobivalent targeting PSMA and FAP are regarded as a strategy offering promise for both the diagnosis and therapy of malignant tumors.

Hu *et al.*⁵⁵ designed and synthesized two new ^{18}F -labeled dual-targeting PSMA/FAP heterodimeric probes, NOTA-PSMA-FAPI-01 and NOTA-PSMA-FAPI-02 (numbers 11 and 12, respectively, in Table 1). In A549-FAP (FAP-

positive) tumor-bearing mice, tumor uptake of the two heterodimers at 120 min (6.4–6.5%ID/g) was considerably superior to that of the monomer $[^{18}\text{F}]\text{FAPI-42}$ (5.25%ID/g). After co-injection with the FAP blocker DOTA-FAPI-04, tumor uptake was almost eliminated. In 22Rv1 (PSMA-positive) tumor-bearing mice, the heterodimers (12.4–12.9%ID/g) also showed distinctly higher tumor uptake than the monomer $[^{18}\text{F}]\text{AlF-PSMA-BCH}$ (6.44%ID/g), and their tumor uptake decreased remarkably following co-administration of the PSMA inhibitor 2-PMPA. These two ^{18}F -labeled PSMA/FAP heterodimers present excellent dual-targeting specificity and achieve greater tumor uptake than single-target probes (Figure 11).⁵⁵

Boinapally *et al.*⁵⁶ synthesized ^{64}Cu -labeled FP-L1 and FP-L2 probes (numbers 13 and 14, respectively, in Table 1). FP-L1, equipped with a polyethylene glycol chain, exhibited increased tumor accumulation and decreased

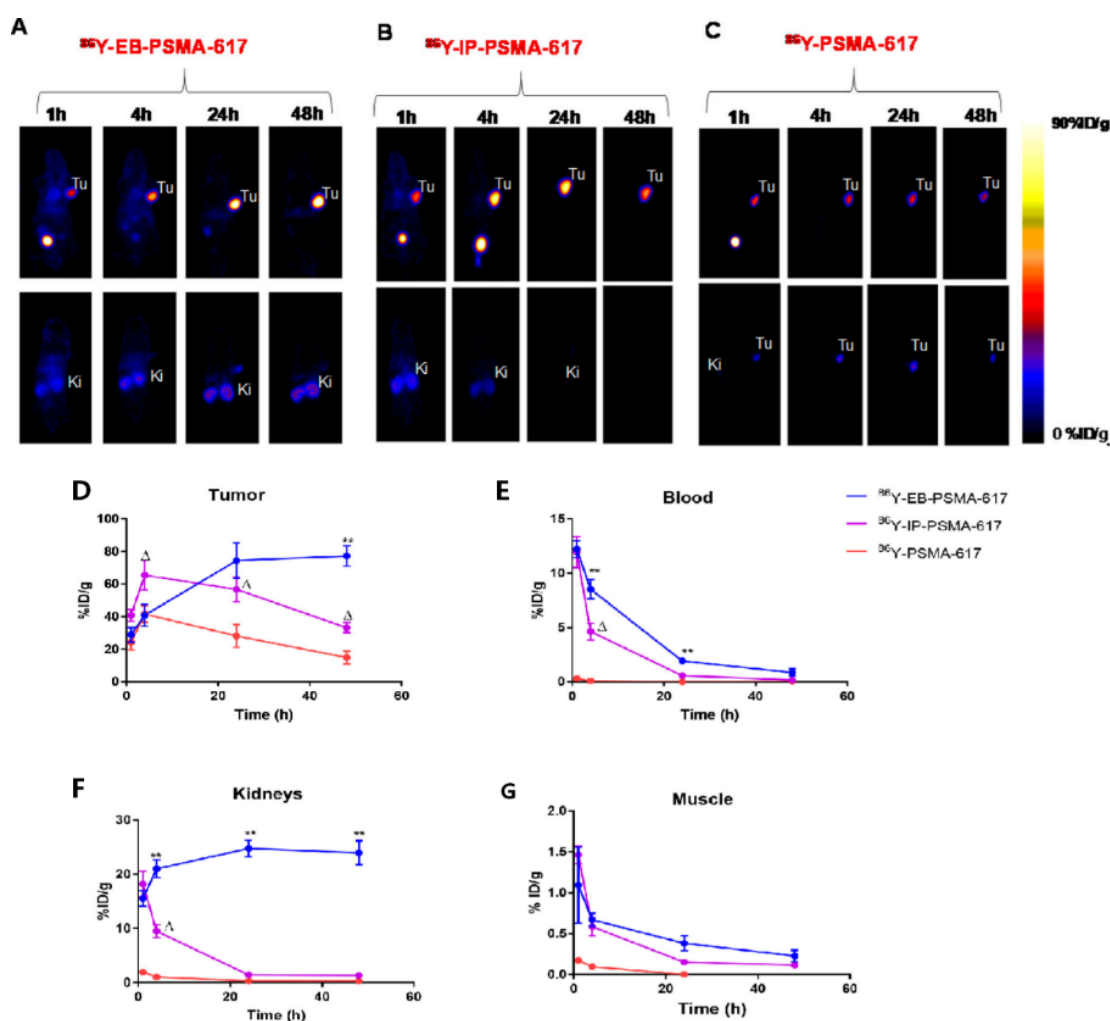


Figure 9. Typical coronal positron emission tomography (PET) images acquired over time in the PSMA-positive tumor model following injection of 3–3.7 MBq of [⁸⁶Y]Y-EB-PSMA-617 (A), [⁸⁶Y]Y-IP-PSMA-617 (B), or [⁸⁶Y]Y-PSMA-617 (C). The upper row shows ventral slices, while the lower row displays dorsal slices. All PET images were normalized to percent injected dose per gram (%ID/g), with a scale ranging from 0 to 90. Decay-corrected time–activity curves for [⁸⁶Y]Y-EB-PSMA-617, [⁸⁶Y]Y-IP-PSMA-617, and [⁸⁶Y]Y-PSMA-617 in the PSMA-positive tumor model are shown for tumor (D), blood (E), kidneys (F), and muscle (G). Reprinted with permission from Wang *et al.*⁵¹ Copyright © 2018 American Chemical Society. Abbreviations: Tu: Tumor; Ki: Kidney.

kidney uptake compared to FP-L2. [⁶⁴Cu]Cu-FP-L1 possesses favorable targeting ability and pharmacokinetic characteristics. To address the issue of tumor heterogeneity in prostate cancer, Wang *et al.*⁵⁷ developed a dual-targeted probe, [⁶⁸Ga]Ga-PSFA-01 (number 15 in Table 1), that simultaneously targets FAP and PSMA, with the PSMA-specific pharmacophore being Glu-urea-Lys (EuK) and the FAP-specific pharmacophore being a quinoline-based scaffold. In first-in-human clinical trials with mCPRC patients, [⁶⁸Ga]Ga-PSFA-01 identified 21 lesions, including primary tumors, skeletal metastases, and lymph node metastases. In contrast, [⁶⁸Ga]Ga-PSMA-11 and [⁶⁸Ga]

Ga-FAPI-04 detected only 13 and 3 lesions, respectively. Preclinical and clinical data have confirmed that [⁶⁸Ga]Ga-PSFA-01 exhibits markedly enhanced tumor lesion detection efficacy compared to single-target probes.

Wang *et al.*⁵⁸ developed a dual-targeted PET imaging radiotracer FAPI-PSMA (number 16 in Table 1) by conjugating PSMA-617 and FAPI-04 to a DOTA chelator via a thiol-maleimide linker. In single-tumor models, the SUV_{max} of [⁶⁸Ga]Ga-FAPI-PSMA in PSMA-positive 22Rv1 tumors reached 1.32, which was considerably greater than 0.45 in PSMA-negative PC3 tumors. The SUV_{max} of FAP-positive U87 MG tumors was 1.67, prominently elevated

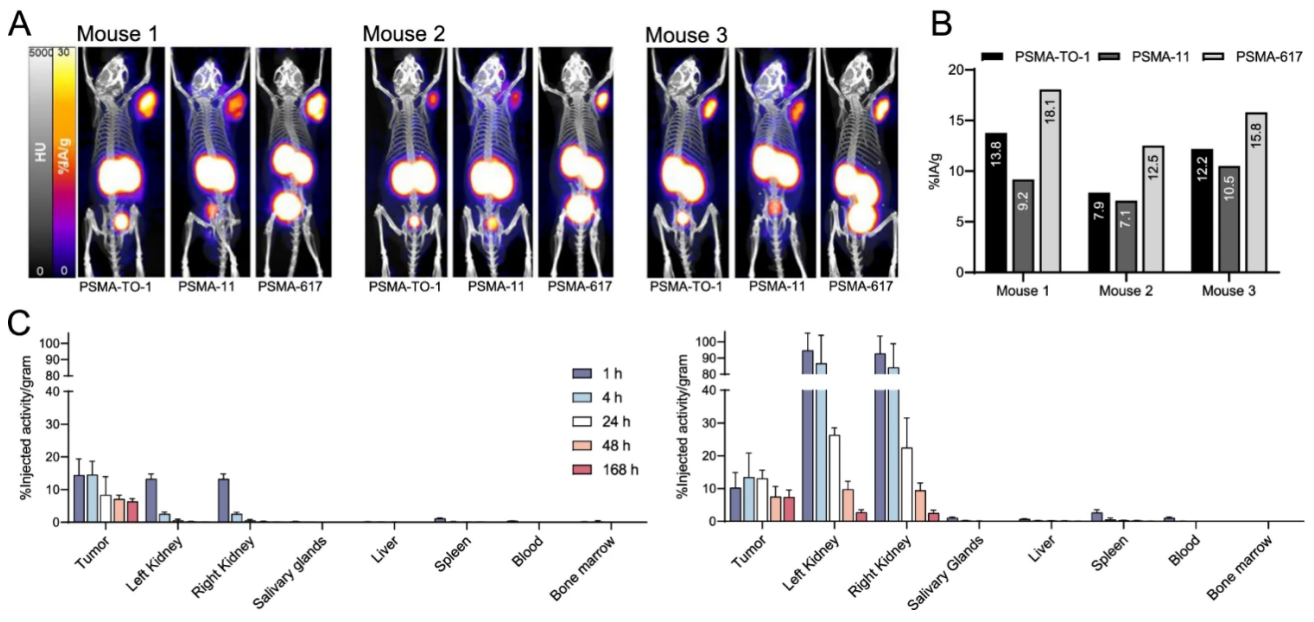


Figure 10. ^{68}Ga /Ga-PSMA positron emission tomography (PET) imaging and ^{177}Lu /Lu-PSMA biodistribution studies in mice. (A) The same three mice bearing subcutaneous C4-2 tumors underwent PET scans at 1 h after injection of ^{68}Ga /Ga-PSMA-TO-1, ^{68}Ga /Ga-PSMA-11, and ^{68}Ga /Ga-PSMA-617 on three consecutive days. (B) Respective tumor uptake expressed as percent injected activity per gram of tissue (%IA/g). The mean tumor uptake values for PSMA-TO-1, PSMA-11, and PSMA-617 were 11.27, 8.92, and 15.46 %IA/g, respectively, with no statistically significant difference among them ($p > 0.06$). (C) Non-decay-corrected %IA/g in tumors and organs of mice administered 30 MBq of ^{177}Lu /Lu-PSMA-617 (left panels) or 30 MBq of ^{177}Lu /Lu-PSMA-TO-1 (right panels) ($n = 5$ mice per time point per ligand; bar graphs represent mean \pm SD). Reprinted from Meyer *et al.*⁵⁴

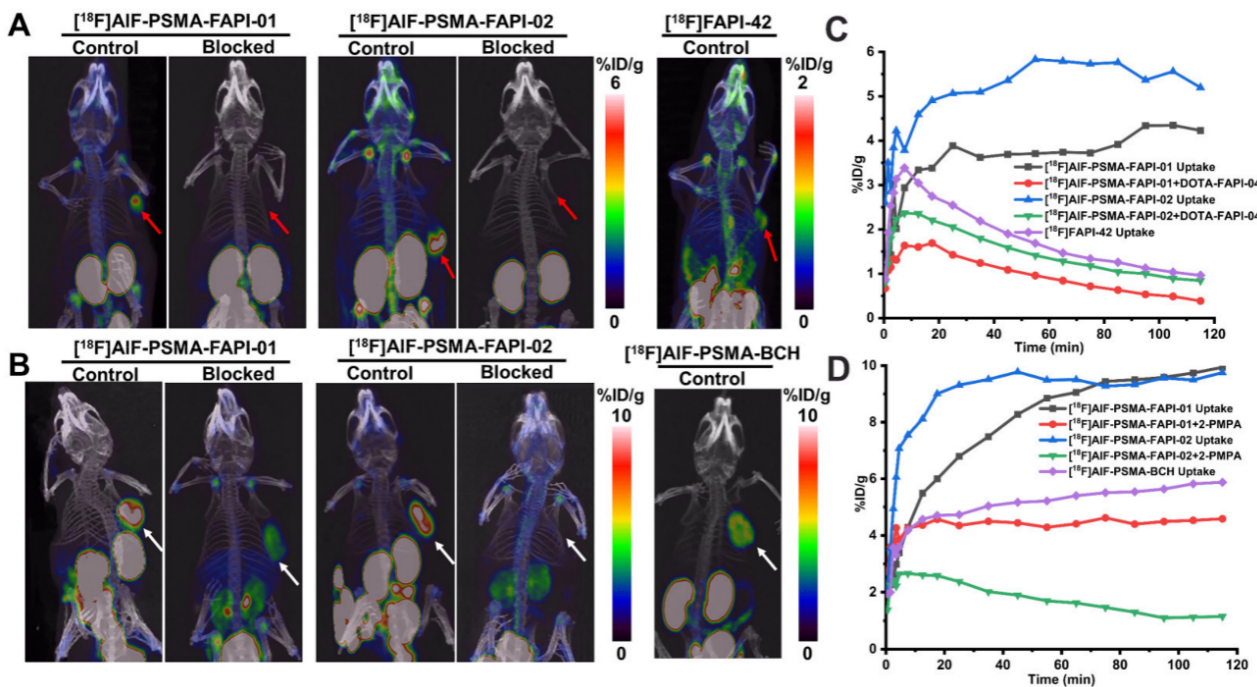


Figure 11. Maximum intensity projection (MIP) images acquired at 15, 30, 60, and 120 min post-injection of ^{18}F AIF-NOTA-PSMA-FAPI-01 (A) and ^{18}F AIF-NOTA-PSMA-FAPI-02 (B) in A549-FAP tumor-bearing mice. The positions of the A549-FAP tumors are indicated by arrows and circles. Time-activity curves for ^{18}F AIF-NOTA-PSMA-FAPI-01 (C) and ^{18}F AIF-NOTA-PSMA-FAPI-02 (D) in selected organs over a 120-min period. Reprinted from Hu *et al.*⁵⁵

compared with 0.70 in FAP-negative A549 tumors. In the bilateral tumor model (22Rv1 + U87 MG), both tumor types were clearly visualized, with SUV_{max} values of 2.92 for 22Rv1 and 1.68 for U87 MG, respectively (Figure 12A, right). In comparison with single-target probes, [^{68}Ga]Ga-PSMA-617 yielded an SUV_{max} of only 0.25 in 22Rv1 tumors, and [^{68}Ga]Ga-FAPI-04 showed an SUV_{max} of merely 0.45 in U87 MG tumors. By contrast, the dual-target probe displayed substantially higher tumor uptake in the same model, with values of 1.32 in 22Rv1 and 0.82 in U87 MG (Figure 12). Moreover, the dual-target probe presented significantly superior tumor-to-heart (T/H) and tumor-to-kidney (T/K) ratios relative to the negative control group.

To improve the selectivity, stability, and pharmacokinetic properties of single-target radiotracers, Hou *et al.*⁵⁹ designed and synthesized two novel ^{68}Ga -labeled PSMA/FAP dual-targeting heterodimeric probes: [^{68}Ga]Ga-PSMA-FAPI-01 (number 17 in Table 1; using FAP-2286 as the FAP-targeting moiety) and [^{68}Ga]Ga-PSMA-FAPI-02 (number 18 in Table 1; using FAPI-04 as the FAP-targeting moiety). In the LNCaP model, the tumor uptake of [^{68}Ga]Ga-PSMA-FAPI-01 ($19.0 \pm 0.6\%$ ID/g) was comparable to that of [^{68}Ga]Ga-PSMA-11 ($18.7 \pm 0.9\%$ ID/g) and [^{68}Ga]Ga-PSMA-I&T ($17.8 \pm 1.1\%$ ID/g), while [^{68}Ga]Ga-PSMA-FAPI-02 exhibited slightly lower tumor uptake ($11.6 \pm 0.5\%$ ID/g). In the U87 tumor model, the tumor uptake of the two dual-target probes ($7.8 \pm 0.4\%$ ID/g and $11.7 \pm 0.5\%$ ID/g, respectively) was equivalent to that of [^{68}Ga]Ga-FAPI-04 ($10.7 \pm 1.53\%$ ID/g) (Figure 13). First-in-human PET/CT imaging (1 h after injection) of [^{68}Ga]Ga-PSMA-FAPI-01 and [^{68}Ga]Ga-PSMA-FAPI-02 was performed in two treatment-naïve prostate cancer patients. The primary prostate tumor was clearly visualized in Patient 1 (Figure 14 left), while relatively low tumor uptake was observed in Patient 2 (Figure 14 right). Meanwhile, retention in non-target organs, especially the liver and salivary glands, was markedly reduced, thereby improving the tumor-to-background ratio (Figure 14).

Wang *et al.*⁶⁰ developed a novel dual-targeted SPECT tracer, [^{99m}Tc]Tc-HFaPSMA (number 21 in Table 1), in which ^{99m}Tc is chelated via 6-hydrazinonicotinic acid (HYNIC) and a symmetric PEG4 linker connects the PSMA-targeting moiety PhPSMA and the FAP-targeting moiety GFAP. In PSMA/FAP-positive 22Rv1+F3 tumor-bearing mice, the heterodimeric tracer [^{99m}Tc]Tc-HFaPSMA mainly accumulated in tumor tissues with an uptake of $16.00 \pm 3.52\%$ ID/g, accompanied by moderate uptake in the kidneys and bladder. Its tumor-targeting efficacy was comparable to that of [^{99m}Tc]Tc-HPSMA ($10.91 \pm 1.08\%$ ID/g; number 20 in Table 1). In contrast, [^{99m}Tc]

Tc-HGFAP (number 19 in Table 1) underwent rapid in vivo excretion and exhibited extremely low tumor uptake ($5.46 \pm 0.62\%$ ID/g). Moreover, the heterodimeric probe presented lower non-target uptake in the submandibular glands, blood, spleen, and other normal tissues than the corresponding single-target tracers (Figure 15).

Based on first-in-human SPECT imaging for Patient 1 (78 years old), both [^{18}F]FDG PET/CT (Figure 16A) and [^{99m}Tc]Tc-HFaPSMA SPECT/CT (Figure 16B) clearly depicted metastatic lesions in the 9th thoracic vertebra (T9), retroperitoneal lymph nodes, and the left acetabulum, with highly consistent lesion localization between the two imaging modalities. In the case of Patient 2 (63 years old), [^{18}F]F-PSMA-1007 PET/CT (Figure 16C) and [^{99m}Tc]Tc-HFaPSMA SPECT/CT (Figure 16D) showed favorable concordance and successfully identified metastatic lesions in the right supraclavicular lymph nodes.⁶⁰

2.2.2. Prostate-specific membrane antigen–gastrin-releasing peptide receptor heterodimer

Belonging to the bombesin receptor family, the gastrin-releasing peptide receptor (GRPR) is a G-protein-coupled receptor. It is widely distributed in the central nervous system and gastrointestinal tract. By recognizing its ligand, gastrin-releasing peptide, GRPR regulates physiological functions such as gastrointestinal hormone secretion and smooth muscle contraction. This receptor is abnormally upregulated in a wide range of human malignancies, especially in prostate cancer with local relapse following internal radiotherapy and external radiation therapy.⁷³

Liolios *et al.*⁶¹ designed and synthesized a bispecific PSMA/GRPR heterodimer RM2-PSMA-617 (number 22 in Table 1), composed of PSMA-617 and the GRPR antagonist RM2 linked via a DOTA chelator (Ga-3). This heterodimeric tracer achieves enhanced tumor accumulation and reduced renal concentration in PSMA-positive tumors, highlighting the advantages of the dual-targeting design. However, its performance in GRPR-positive tumors is limited by GRPR expression levels and ligand binding affinity.

Mitran *et al.*⁶² synthesized the heterodimeric NOTA-DUPA-RM26 (number 23 in Table 1) via manual solid-phase peptide synthesis. Subsequent microPET/CT and microSPECT/CT imaging demonstrated that both radiotracers clearly visualize tumors at 1 h with low renal background signal. The tumor-to-background ratio increased progressively up to 3 h. Moreover, the ^{111}In -labeled conjugate exhibited higher tumor uptake ($12 \pm 2\%$ ID/g versus $8 \pm 2\%$ ID/g for the ^{68}Ga -labeled agent) and slower in vivo clearance. In PIP-PC3 (PSMA⁺/GRPR⁺) tumor-bearing mice, simultaneous blockade of PSMA

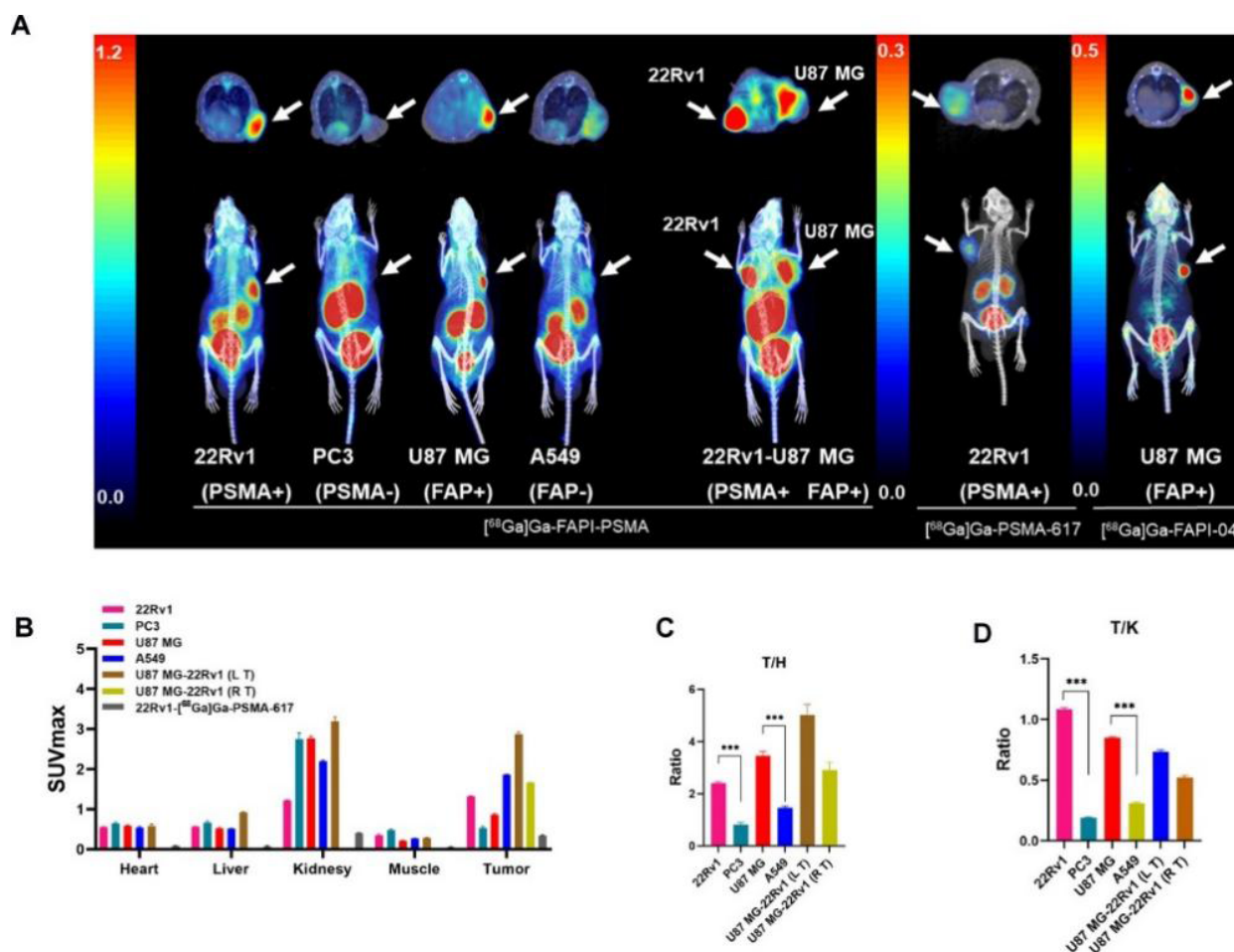


Figure 12. Positron emission tomography/computed tomography (PET/CT) images, maximum standardized uptake value (SUV_{max}), and tumor-to-organ ratios in tumor-bearing mice. (A) [⁶⁸Ga]Ga-FAPI-PSMA PET/CT images of mice bearing 22Rv1, PC3, U87 MG, A549, or both 22Rv1 and U87 MG tumors; [⁶⁸Ga]Ga-PSMA-617 images of mice bearing 22Rv1; and [⁶⁸Ga]Ga-FAPI-04 images of mice bearing U87 MG. (B) Comparison of SUV_{max} across the six groups of xenograft-bearing mice based on regions of interest. (C) Tumor-to-heart (T/H) ratios. (D) Tumor-to-kidney (T/K) ratios. Reprinted with permission from Wang *et al.*⁵⁸ Copyright © 2023 American Chemical Society.

and GRPR significantly reduced tumor uptake, validating the dual-targeting capability of this heterodimer in vivo (Figure 17).

By employing shorter polyethylene glycol and carbon chain segments than NOTA-DUPA-RM26, Lundmark *et al.*⁶³ developed BQ7812 (number 24 in Table 1). At 1 h after injection of [¹¹¹In]In-BQ7812, tumors were clearly visualized with an uptake of 16.1%ID/g. By 3 h post-administration, background radioactivity in normal tissues decreased markedly, leading to superior tumor contrast (Figure 18). With rational structural optimization, BQ7812 possesses enhanced PSMA binding affinity while retaining rapid systemic clearance and a high tumor-to-background ratio, making it a promising PSMA/GRPR

dual-targeted SPECT imaging agent.

2.2.3. Prostate-specific membrane antigen-somatostatin receptor 2 Heterodimer

Somatostatin receptor 2 (SSTR2), a G-protein-coupled receptor, belongs to the somatostatin receptor family. Its primary function is to regulate cell proliferation, hormone secretion, and signal transduction by binding to endogenous somatostatin or exogenous somatostatin analogs. Existing studies have revealed that NEPC tumors with low PSMA expression exhibit strong uptake of SSTR2-targeted ligands, DOTA-1-Nal³-octreotide (DOTA-NOC) and DOTA-Tyr³-octreotate (DOTA-TATE). This finding supports the development of dual-targeted radioligands targeting both PSMA and SSTR2.

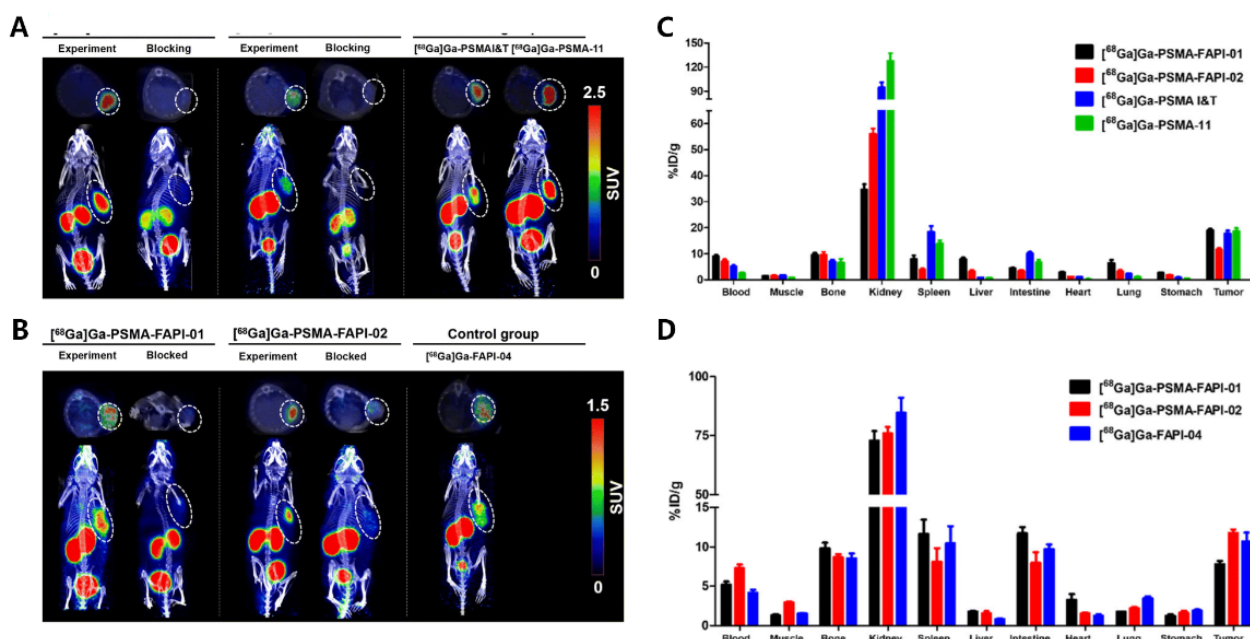


Figure 13. Micro-positron emission tomography (PET) images of $[^{68}\text{Ga}]\text{Ga-PSMA-FAPI-01}$ and $[^{68}\text{Ga}]\text{Ga-PSMA-FAPI-02}$ were acquired at 1.5 h post-injection. (A) $[^{68}\text{Ga}]\text{Ga-PSMA-11}$ and $[^{68}\text{Ga}]\text{Ga-PSMA-I\&T}$ served as reference controls in LNCaP tumor-bearing mice. (B) $[^{68}\text{Ga}]\text{Ga-FAPI-04}$ was used as a comparator in U87 tumor-bearing mice. For blocking experiments, mice received co-injection of the radiotracers together with an excess of either PSMA-I&T or FAPI-04. White circles denote the tumor locations. Transverse (cross-sectional) images are also shown to facilitate clearer tumor visualization. (C) Biodistribution profiles of the two novel radiotracers at 1.5 h in the LNCaP xenograft model, compared with those of $[^{68}\text{Ga}]\text{Ga-PSMA-11}$ and $[^{68}\text{Ga}]\text{Ga-PSMA-I\&T}$. (D) Biodistribution profiles of the two novel radiotracers at 1.5 h in the U87 xenograft model, compared with that of $[^{68}\text{Ga}]\text{Ga-FAPI-04}$. Reprinted with permission from Hou *et al.*⁵⁹ Copyright © 2024 Royal Society of Chemistry.

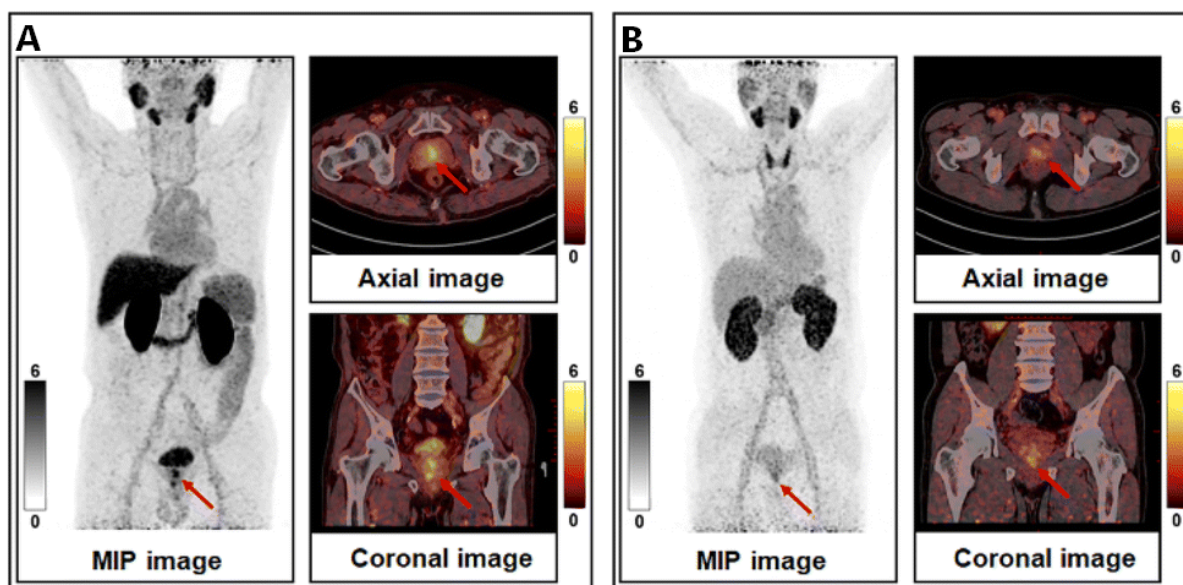


Figure 14. Positron emission tomography (PET) maximum intensity projection (MIP) and corresponding PET/computed tomography (CT) fusion (axial and coronal) of $[^{68}\text{Ga}]\text{Ga-PSMA-FAPI-01}$ (A) and $[^{68}\text{Ga}]\text{Ga-PSMA-FAPI-02}$ (B) at 1 h post-injection are presented. Prostate cancer lesions are marked by red arrows. Reprinted with permission from Hou H *et al.*⁵⁹ Copyright © 2024 Royal Society of Chemistry.

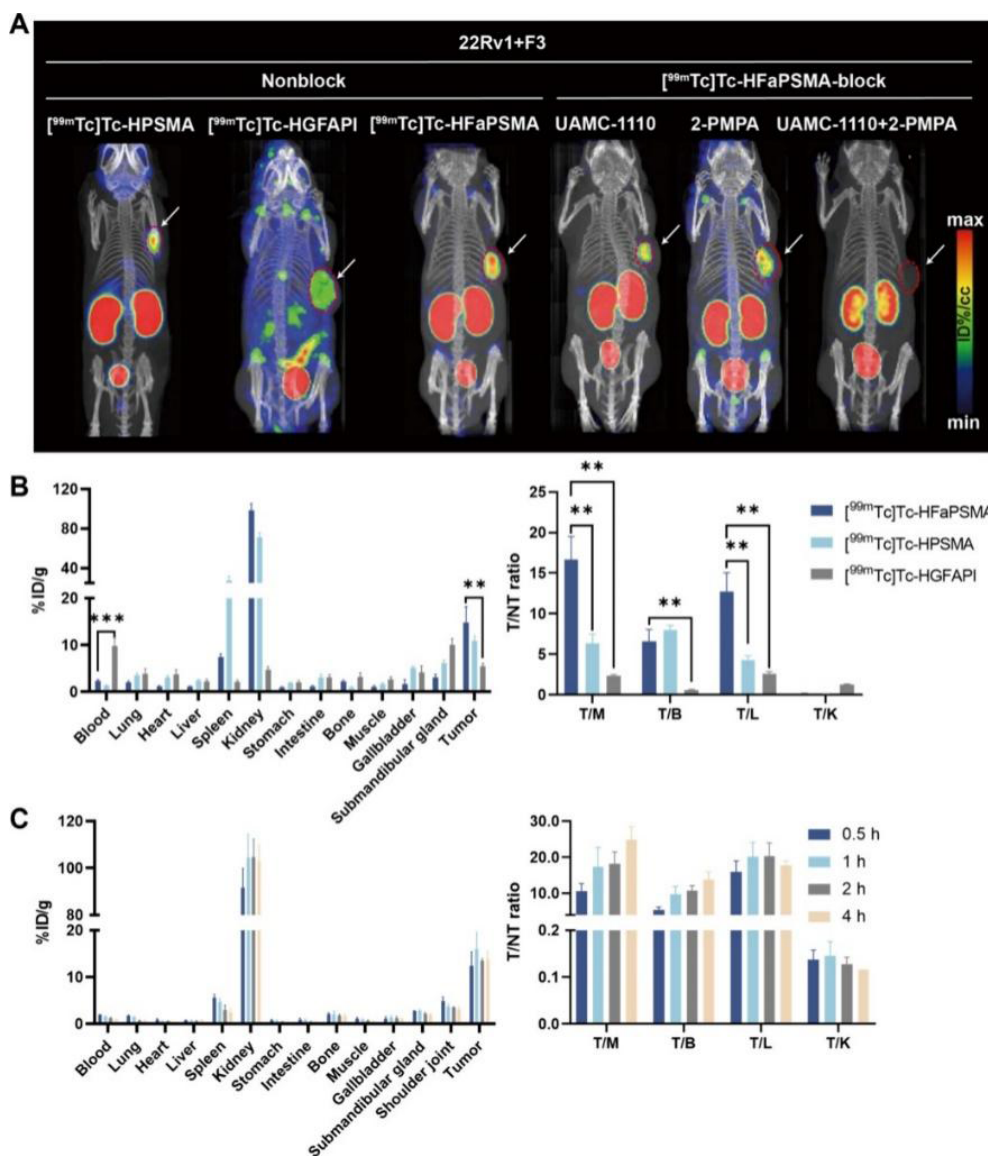


Figure 15. Maximum-intensity-projection (MIP) single-photon emission computed tomography/computed tomography (SPECT/CT) images and biodistribution data for $[^{99m}\text{Tc}]\text{Tc-HPSMA}$, $[^{99m}\text{Tc}]\text{Tc-HGFAPI}$, and $[^{99m}\text{Tc}]\text{Tc-HFaPSMA}$ in BALB/c nude mice carrying both 22Rv1 and F3 xenografts. (A) SPECT/CT images at 1 h post-injection demonstrate the radiotracer distribution characteristics, including blocking studies with $[^{99m}\text{Tc}]\text{Tc-HFaPSMA}$ coinjected with UAMC-1110, 2-PMPA, or their combination. (B) Biodistribution profiles (expressed as %ID/g) and tumor-to-normal tissue ratios (tumor/muscle, blood, liver, and kidney) at 1 h post-injection. (C) Time-dependent biodistribution and tumor-to-healthy tissue ratios of $[^{99m}\text{Tc}]\text{Tc-HFaPSMA}$ at 0.5, 1, 2, and 4 h post-injection. Reprinted with permission from Wang *et al.*⁶⁰ Copyright © 2025 American Chemical Society.

Jin *et al.*⁶⁴ designed and synthesized two dual-targeted theranostic probes targeting PSMA and SSTR2: $[^{68}\text{Ga}]\text{Ga-PSMA-SSTR2-1}$ and $[^{68}\text{Ga}]\text{Ga}/[^{177}\text{Lu}]\text{Lu-PSMA-SSTR2-1}$ (numbers 25 and 26, respectively, in Table 1). At 60 min post-injection in 22Rv1 tumors, the retention values of $[^{68}\text{Ga}]\text{Ga-PSMA-SSTR2-1}$, $[^{68}\text{Ga}]\text{Ga-PSMA-SSTR2-2}$, and $[^{177}\text{Lu}]\text{Lu-PSMA-SSTR2-2}$ were 15.47 ± 3.35 , 17.67 ± 4.26 , and $28.34 \pm 5.18\%$ ID/g, respectively, and their tumor

uptake was significantly blocked by PSMA inhibitors. $[^{68}\text{Ga}]\text{Ga-PSMA-SSTR2-2}$ exhibited faster blood clearance, with a blood radioactivity level of $6.84 \pm 0.69\%$ ID/g, compared with $9.69 \pm 0.32\%$ ID/g for $[^{68}\text{Ga}]\text{Ga-PSMA-SSTR2-1}$. In H69 tumors, the uptake of $[^{68}\text{Ga}]\text{Ga-PSMA-SSTR2-2}$ and $[^{177}\text{Lu}]\text{Lu-PSMA-SSTR2-2}$ reached $11.93 \pm 0.83\%$ ID/g and $15.38 \pm 3.29\%$ ID/g, respectively, and these signals were also effectively inhibited by SSTR2 antagonists

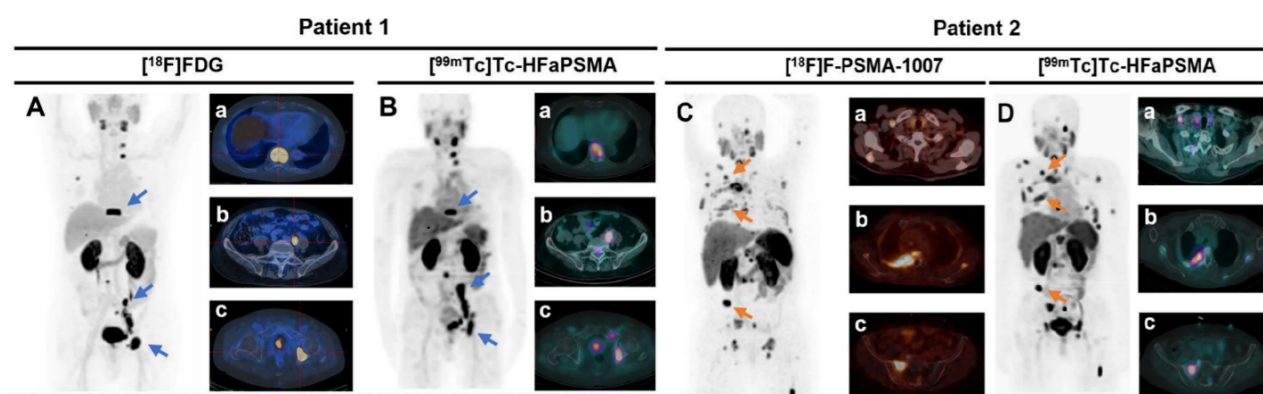


Figure 16. Positron emission tomography/computed tomography (PET/CT) and single-photon emission computed tomography (SPECT)/CT images of two prostate cancer patients. Maximum-intensity-projection (MIP) images and three representative merged transverse images of $[^{18}\text{F}]\text{FDG}$ (A) and $[^{99\text{m}}\text{Tc}]\text{Tc-HFaPSMA}$ (B) in a 78-year-old patient. Fused axial image showing thoracic nine cone metastases (a), retroperitoneal lymph nodes (b), and left acetabulum (c). MIP images of $[^{18}\text{F}]\text{F-PSMA-1007}$ (C) and $[^{99\text{m}}\text{Tc}]\text{Tc-HFaPSMA}$ (D) in a 63-year-old patient. Fused axial image showing the right supraclavicular fossa lymph node (a), the right 3 posterior ribs (b), and the right sacroiliac joint (c). Arrows from top to bottom correspond to the right fusion axial image. Reprinted with permission from Wang *et al.*⁶⁰ Copyright © 2025 American Chemical Society.

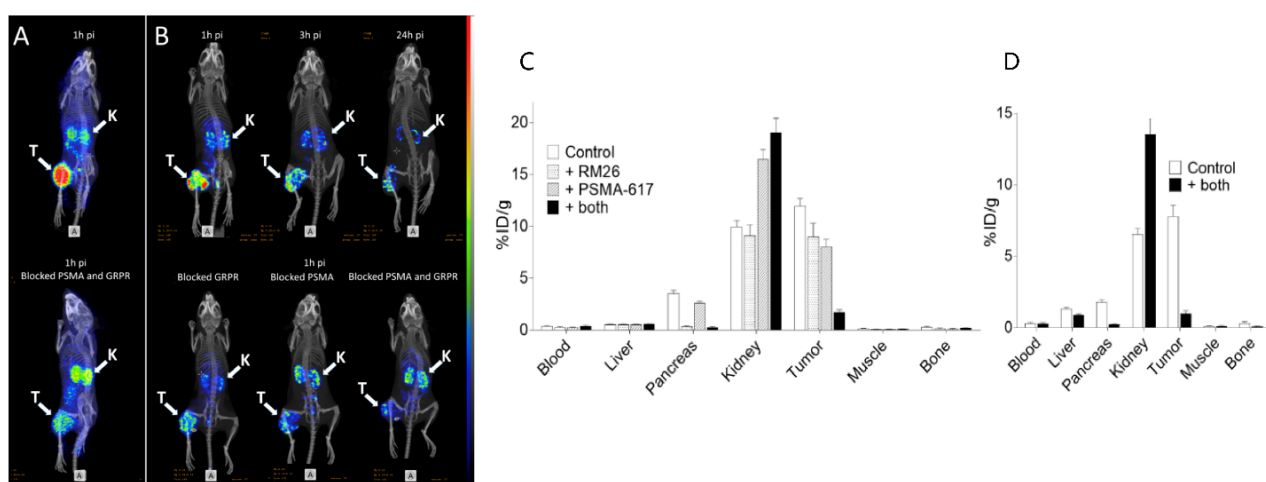


Figure 17. Single-photon emission computed tomography/computed tomography (SPECT/CT) images and biodistribution profiles of PC3-PIP xenograft mice. Maximum intensity projection (MIP) images from (A) micro-positron emission tomography (microPET)/CT and (B) microSPECT/CT of PC3-PIP xenograft-bearing mice (PSMA⁺/GRPR⁺) following intravenous injection of $[^{68}\text{Ga}]\text{Ga-NOTA-DUPA-RM26}$ and $[^{111}\text{In}]\text{In-NOTA-DUPA-RM26}$. For blocking experiments, animals received co-injections of PSMA-617 (to block PSMA), RM26 (to block GRPR), or both agents. In vivo specificity of (C) $[^{111}\text{In}]\text{In-NOTA-DUPA-RM26}$ and (D) $[^{68}\text{Ga}]\text{Ga-NOTA-DUPA-RM26}$ evaluated in BALB/c nu/nu mice bearing PC3-PIP xenografts at 1 h post-injection. Mice were administered intravenously with 50 pmol of the respective radiotracer, either alone or in combination with 1.5 nmol of non-labeled RM26, 1.5 nmol of non-labeled PSMA-617, or both. Tissue radioactivity uptake was expressed as a percentage of injected dose per gram of tissue (%ID/g). Data are presented as mean \pm SD. Reprinted from Mitran *et al.*⁶²

(Figure 19). Therefore, both dual-targeted probes display favorable targeting specificity toward PSMA and SSTR2, as well as potent tumor accumulation capacity.

2.2.4. Prostate-specific membrane antigen–neurotensin receptor heterodimer

In addition to the expression of SSTR2, NEPC is also

closely correlated with the expression of neurotensin receptors (NTSRs), particularly in PSMA-negative NEPC. NTSRs are defined as GPCRs that serve as receptors for the neuropeptide neurotensin. They have essential functions in multiple physiological and pathological pathways, including nervous system regulation, gastrointestinal function, and tumorigenesis. In advanced prostate cancer, especially

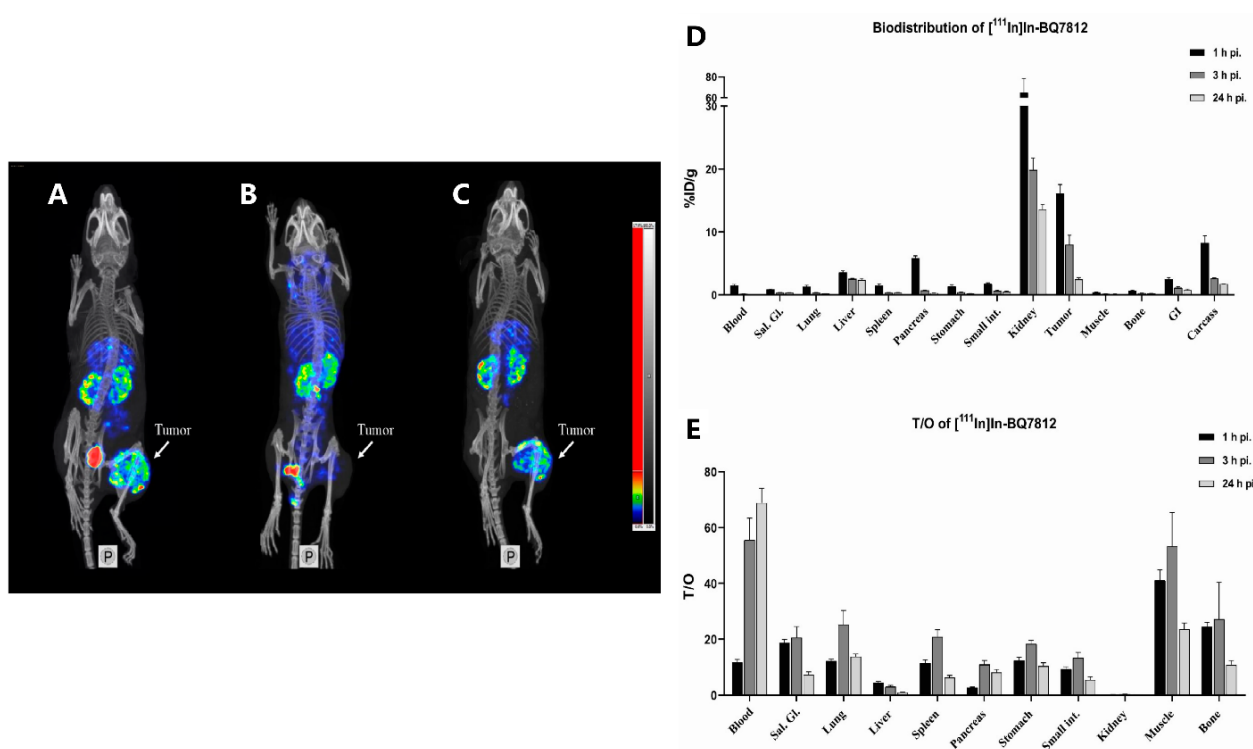


Figure 18. NanoScan single-photon emission computed tomography/computed tomography (SPECT/CT) images of PC3-pip tumor-bearing mice acquired after injection of [¹¹¹In]In-BQ7812. (A) Unblocked group at 1 h post-injection (pi.). (B) Blocked group at 1 h post-injection following co-administration of non-labeled PSMA-11 and NOTA-PEG4-RM26. (C) Unblocked group at 3 h pi. (D) Biodistribution profile of [¹¹¹In]In-BQ7812 in PC3-pip tumor-bearing mice at 1, 3, and 24 h pi. (E) Tumor-to-healthy organ ratios of [¹¹¹In]In-BQ7812 at 1, 3, and 24 h pi. Reprinted from Lundmark *et al.*⁶³

under long-term ADT conditions, neuroendocrine cell populations around prostate tumors specifically bind to NTSR1. As an alternative androgen-independent growth factor, NTSR1 promotes the continuous growth of tumors.⁷⁴ Based on this rationale, Ma *et al.*⁶⁵ designed and synthesized a bispecific heterodimer [¹⁸F]F-BCN-PSMA-NT (number 27 in Table 1). The heterodimer [¹⁸F]F-BCN-PSMA-NT enabled clear tumor visualization in both PC-3 (NTSR1⁺/PSMA⁻) and LNCaP (PSMA⁺/NTSR1⁻) tumor-bearing mice. At 40 min post-injection, the tumor uptake values were $1.4 \pm 0.3\%ID/g$ and $1.3 \pm 0.2\%ID/g$, respectively, and were significantly inhibited by corresponding blocking agents. The monomer [¹⁸F]F-BCN-NT only visualized PC-3 tumors with an uptake of $1.2 \pm 0.3\%ID/g$ and showed negligible accumulation in LNCaP tumors. Meanwhile, the monomer [¹⁸F]F-BCN-PSMA yielded distinct imaging signals solely in LNCaP tumors and presented no uptake in PC-3 tumors (Figure 20).

These results demonstrate that the dual-targeted probe

is able to simultaneously identify heterogeneous tumor lesions with PSMA or NTSR1 expression, whereas single-targeted monomers only detect their respective receptor-positive tumors. Accordingly, the superior potential of the dual-targeting strategy in overcoming heterogeneity of prostate cancer was fully validated.

3. Discussion

The emerging PSMA-targeted radioligand therapy exhibits high targeting precision and prominent theranostic potential. It delivers significant survival benefits to patients with mCRPC and high PSMA expression, while avoiding widespread systemic damage induced by conventional radiotherapy. However, this therapeutic modality remains in the early research phase and has notable limitations.

Methodologically, there is no standardized PET/SPECT acquisition protocol for PSMA-targeted radioligand therapy. Variations in imaging time points, injected activity, reconstruction algorithms, and SUV quantification

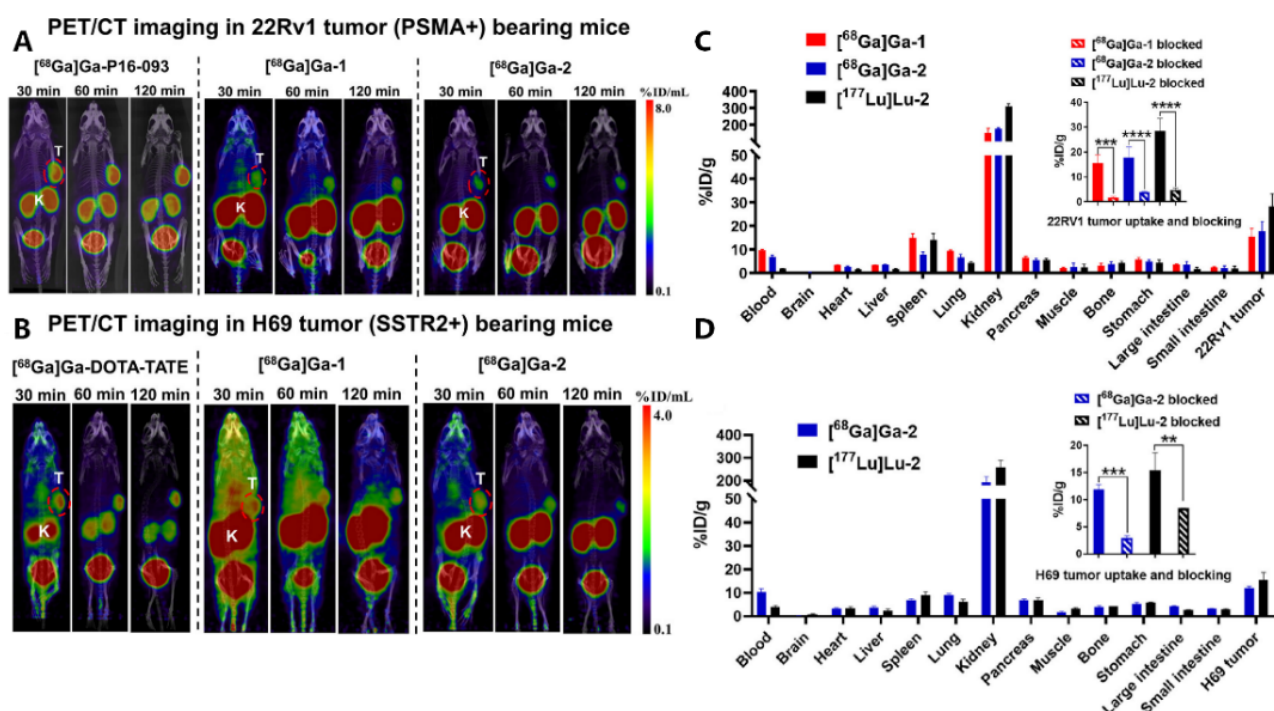


Figure 19. Positron emission tomography/computed tomography (PET/CT) imaging and biodistribution profiles of tumor-bearing mice. (A) PET/CT images of $[^{68}\text{Ga}]\text{Ga-P16-093}$, $[^{68}\text{Ga}]\text{Ga-PSMA-SSTR2-1}$ ($[^{68}\text{Ga}]\text{Ga-1}$), and $[^{68}\text{Ga}]\text{Ga-PSMA-SSTR2-2}$ ($[^{68}\text{Ga}]\text{Ga-2}$) in 22Rv1 (PSMA⁺) tumor-bearing mice. (B) PET/CT images of $[^{68}\text{Ga}]\text{Ga-DOTA-TATE}$, $[^{68}\text{Ga}]\text{Ga-1}$, and $[^{68}\text{Ga}]\text{Ga-2}$ in H69 (SSTR2⁺) tumor-bearing mice. (C) Biodistribution data of $[^{68}\text{Ga}]\text{Ga-1}$, $[^{68}\text{Ga}]\text{Ga-2}$, and $[^{177}\text{Lu}]\text{Lu-PSMA-SSTR2-2}$ ($[^{177}\text{Lu}]\text{Lu-2}$) in 22Rv1 tumor-bearing mice. For blocking studies, unlabeled PSMA-11 (12 nmol/mouse) was co-injected. (D) Biodistribution data of $[^{68}\text{Ga}]\text{Ga-2}$ and $[^{177}\text{Lu}]\text{Lu-2}$ in H69 tumor-bearing mice. Blocking was performed by co-injecting unlabeled DOTA-[Tyr³]-octreotide (DOTA-TOC; 12 nmol/mouse). Reprinted with permission from Jin *et al.*⁶⁴ Copyright © 2025 American Chemical Society. Abbreviations: K: Kidney; T: Tumor.

approaches cause substantial quantitative heterogeneity across studies, hindering direct comparisons among different radioligands. Moreover, mouse tumor models cannot fully recapitulate the immune microenvironment, metastatic characteristics, and tumor heterogeneity of advanced human prostate cancer. Consequently, encouraging preclinical findings may not translate into equivalent therapeutic effects in clinical settings. In addition, current clinical trials are limited by small sample sizes and inter-patient variability, which elevate random statistical errors and render some conclusions statistically insignificant. In several studies, the absence of detailed confidence intervals prevents accurate evaluation of the precision and variation range of effect sizes. A lack of reproducibility analyses compromises the robustness and verifiability of reported results. Failure to implement corrections for multiple statistical comparisons substantially elevates the risk of false-positive findings arising from repeated hypothesis testing.

In terms of PSMA pathophysiology, heterogeneity in

tumor PSMA expression—particularly following long-term ADT or neuroendocrine differentiation—constitutes a major barrier to treatment failure and drug resistance. PSMA-negative or low-expression lesions keep progressing due to off-target effects. Furthermore, PSMA is expressed in normal tissues such as salivary glands, parotid glands, and submandibular glands, leading to radioligand accumulation at these sites. This subsequently triggers adverse events, including xerostomia, fatigue, and dose-limiting nephrotoxicity. Interpatient variations, including renal clearance rate, hepatic metabolic capacity, whole-body tumor burden (which may lead to the sink effect), physical constitution (e.g., body weight and fat distribution altering volume of distribution), as well as intratumoral PSMA receptor density and heterogeneity, substantially govern the pharmacokinetic profile of radiotracers and the absorbed dose delivered to tumor and healthy organs.

Regarding PSMA ligands, urea-based PSMA inhibitors, such as PSMA-617 and PSMA-11, possess high nanomolar affinity for PSMA. They achieve specific tumor uptake

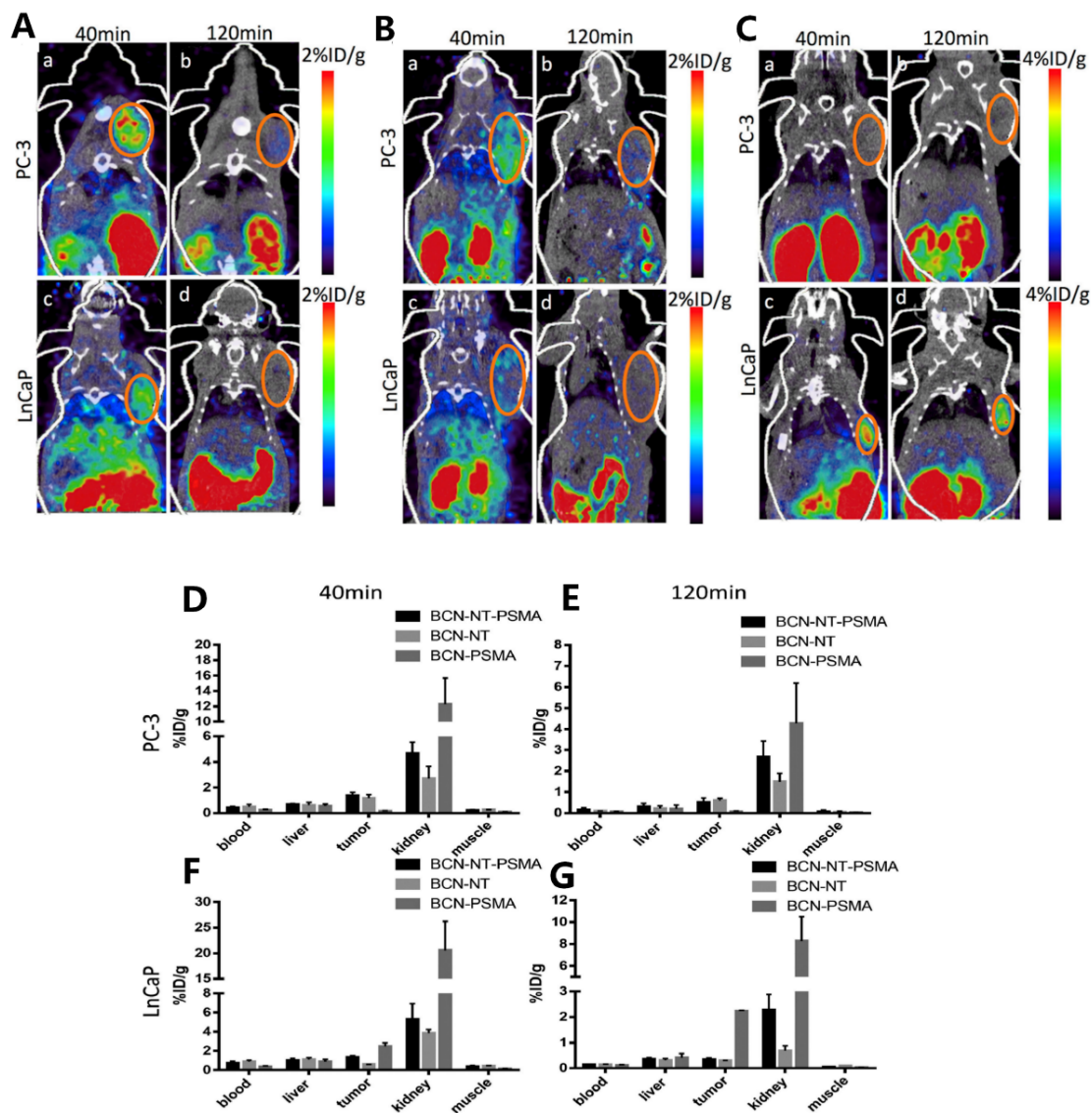


Figure 20. Representative positron emission tomography/computed tomography (PET/CT) images of the $[^{18}\text{F}]\text{-BCN-PSMA-NT}$ heterodimer in PC-3 tumor models acquired at 40 min (A, a) and 120 min (A, b) post-injection. In LnCaP tumor models, images of the same heterodimer are shown at 40 min (A, c) and 120 min (A, d). For the monomer $[^{18}\text{F}]\text{-BCN-NT}$, PET/CT images in PC-3 tumors are displayed at 40 min (B, a) and 120 min (B, b), and in LnCaP tumors at 40 min (B, c) and 120 min (B, d). For the other monomer $[^{18}\text{F}]\text{-BCN-PSMA}$, images in PC-3 tumors are presented at 40 min (C, a) and 120 min (C, b), and in LnCaP tumors at 40 min (C, c) and 120 min (C, d). Quantitative uptake values derived from PET for the BCN-NT-PSMA heterodimer and the corresponding monomers are shown for PC-3 at 40 min (D) and 120 min (E), and for LnCaP at 40 min (F) and 120 min (G). Reprinted with permission from Ma *et al.*⁶⁵ Copyright © 2019 American Chemical Society.

and are rapidly excreted through the kidneys and urinary bladder. Although rapid clearance is favorable for imaging, it limits the total accumulation of these agents in tumor lesions. Structural modification of PSMA ligands by incorporating albumin-binding moieties can prolong their blood circulation time and enhance tumor accumulation.

Nevertheless, this strategy increases renal exposure, thereby raising the risks of severe nephrotoxicity and dose-limiting toxicity. Furthermore, studies reporting positive outcomes of certain PSMA ligands tend to be preferentially published, whereas those with negative or neutral findings are likely underrepresented. Such publication bias may lead

to overestimation of the true therapeutic efficacy. This bias should be carefully considered when interpreting available literature to objectively evaluate the clinical value of PSMA-targeted theranostics regardless of study outcomes.

Despite their promise, dual-targeting ligands can significantly enhance tumor uptake while simultaneously increasing non-target uptake and increasing radiation exposure in the liver, kidneys, and bone marrow. Accordingly, the development of dual-targeted ligands requires a delicate balance between therapeutic efficacy and toxic side effects. Optimizing linker length, tuning the affinity ratio of different targeting moieties, and introducing cleavable functional groups can improve pharmacokinetic profiles and effectively broaden the therapeutic window. Furthermore, dual-targeting molecules require complicated synthetic processes and expensive radionuclides, which impede their routine clinical use. For several promising ligands, long-term follow-up data—including patient survival rates, risks of secondary malignancies, and delayed adverse reactions—remain insufficient to support further clinical evaluation.

4. Conclusion

Research on PSMA-targeted radioligands is advancing at an unprecedented rate. To address tumor heterogeneity associated with PSMA, researchers adopt strategies such as linker optimization, multimerization, and incorporation of albumin-binding moieties to improve tumor uptake and retention. Structural optimization can not only enhance targeting affinity and specificity but also modulate pharmacokinetic properties, such as logD, half-life, absorption, distribution, metabolism, and excretion. Nevertheless, emerging PSMA-targeted radioligands still suffer from non-target organ uptake and off-target toxicity. Meanwhile, ongoing efforts focus on elucidating pharmacodynamic mechanisms, balancing therapeutic efficacy and adverse effects, developing superior therapeutic regimens, optimizing production processes, and promoting the research and development of dual-targeted radiotracers.

Acknowledgments

None.

Funding

This work was funded by the Tianjin Key Scientific Research Program and Clinical Specialty (Oncology, Grant number: 25ZXSWY00200).

Conflict of interest

Dezhao Zhang, Yeting Zheng, Xinyue Ge, and Feihu Guo

are employees of Tianjin Hengrui Pharmaceuticals Co., Ltd., Tianjin, China; however, they were not involved in any activities that could constitute a conflict of interest in relation to this study. The authors declare that they have no conflicts of interest.

Author contributions

Conceptualization: Yeting Zheng, Xinyue Ge, Chun Zhang, Feihu Guo

Funding acquisition: Feihu Guo

Supervision: Yeting Zheng, Xinyue Ge, Chun Zhang, Feihu Guo

Visualization: Dezhao Zhang

Writing—original draft: Dezhao Zhang

Writing—review & editing: Yeting Zheng, Xinyue Ge, Chun Zhang, Feihu Guo

Ethics approval and consent to participate

Not applicable.

Consent for publication

Not applicable.

Availability of data

Not applicable.

References

1. Bray F, Laversanne M, Sung H, *et al.* Global cancer statistics 2022: GLOBOCAN estimates of incidence and mortality worldwide for 36 cancers in 185 countries. *CA Cancer J Clin.* 2024;74:229-263.
doi: 10.3322/caac.21834
2. James ND, Tannock I, N'Dow J, *et al.* The Lancet Commission on prostate cancer: planning for the surge in cases. *Lancet.* 2024;403(10437):1683-1722.
doi: 10.1016/S0140-6736(24)00651-2
3. Chakrabarti D, Albertsen P, Adkins A, *et al.* The contemporary management of prostate cancer. *CA Cancer J Clin.* 2025;75(6):552-586.
doi: 10.3322/caac.70020
4. Malik SS, Batool R, Masood N, Yasmin A. Risk factors for prostate cancer: a multifactorial case-control study. *Curr Probl Cancer.* 2018;42(3):337-343.
doi: 10.1016/j.currprobcancer.2018.01.014
5. Oczkowski M, Dziendzikowska K, Pasternak-Winiarska A, Włodarek D, Gromadzka-Ostrowska J. Dietary factors and prostate cancer development, progression, and reduction. *Nutrients.* 2021;13(2):496.
doi: 10.3390/nu13020496

6. Almeeri MNE, Awies M, Constantinou C. Prostate cancer, pathophysiology and recent developments in management: a narrative review. *Curr Oncol Rep.* 2024;26(11):1511-1519. doi: 10.1007/s11912-024-01614-6
7. Tortorella E, Giantulli S, Sciarra A, Silvestri I. AR and PI3K/AKT in prostate cancer: a tale of two interconnected pathways. *Int J Mol Sci.* 2023;24(3):2046. doi: 10.3390/ijms24032046
8. Tzelepi V. Prostate cancer: pathophysiology, pathology and therapy. *Cancers.* 2022;15(1):281. doi: 10.3390/cancers15010281
9. Jiang S, Li H, Zhang L. Generic Diagramming Platform (GDP): a comprehensive database of high-quality biomedical graphics. *Nucleic Acids Res.* 2025;53(D1):D1670-D1676. doi: 10.1093/nar/gkae973
10. Nikfarjam Z, Zargari F, Nowroozi A, Bavi O. Metamorphosis of prostate specific membrane antigen (PSMA) inhibitors. *Biophys Rev.* 2022;14(1):303-315. doi: 10.1007/s12551-021-00919-1
11. Maes J, Gesquière S, De Spiegeleer A, Maes A, Van de Wiele C. Prostate-specific membrane antigen biology and pathophysiology in prostate carcinoma, an update: potential implications for targeted imaging and therapy. *Int J Mol Sci.* 2024;25(17):9755. doi: 10.3390/ijms25179755
12. Jiao J, Kang F, Zhang J, et al. Establishment and prospective validation of an SUVmax cutoff value to discriminate clinically significant prostate cancer from benign prostate diseases in patients with suspected prostate cancer by 68Ga-PSMA PET/CT: a real-world study. *Theranostics.* 2021;11(17):8396-8411. doi: 10.7150/thno.58140
13. Mei R, Bracarda S, Emmett L, et al. Androgen deprivation therapy and its modulation of PSMA expression in prostate cancer: mini review and case series of patients studied with sequential [68Ga]-Ga-PSMA-11 PET/CT. *Clin Transl Imaging.* 2021;9(3):215-220. doi: 10.1007/s40336-021-00421-4
14. Pabst KM, Mei R, Lückerrath K, et al. Detection of tumour heterogeneity in patients with advanced, metastatic castration-resistant prostate cancer on [68Ga]Ga-/[18F]F-PSMA-11-1007, [68Ga]Ga-FAPI-46 and 2-[18F]FDG PET/CT: a pilot study. *Eur J Nucl Med Mol Imaging.* 2024;52(1):342-353. doi: 10.1007/s00259-024-06891-8
15. Meller B, Bremmer F, Sahlmann CO, et al. Alterations in androgen deprivation enhanced prostate-specific membrane antigen (PSMA) expression in prostate cancer cells as a target for diagnostics and therapy. *EJNMMI Res.* 2015;5(1):66. doi: 10.1186/s13550-015-0145-8
16. Afshar-Oromieh A, Debus N, Uhrig M, et al. Impact of long-term androgen deprivation therapy on PSMA ligand PET/CT in patients with castration-sensitive prostate cancer. *Eur J Nucl Med Mol Imaging.* 2018;45(12):2045-2054. doi: 10.1007/s00259-018-4079-z
17. Maylin ZR, Smith C, Classen A, Asim M, Pandha H, Wang Y. Therapeutic exploitation of neuroendocrine transdifferentiation drivers in prostate cancer. *Cells.* 2024;13(23):1999. doi: 10.3390/cells13231999
18. Bakht MK, Derecichei I, Li Y, et al. Neuroendocrine differentiation of prostate cancer leads to PSMA suppression. *Endocr Relat Cancer.* 2019;26(2):131-146. doi: 10.1530/ERC-18-0226
19. Zaidi S, Park J, Chan JM, et al. Single-cell analysis of treatment-resistant prostate cancer: implications of cell state changes for cell surface antigen-targeted therapies. *Proc Natl Acad Sci U S A.* 2024;121(28):e2322203121. doi: 10.1073/pnas.2322203121
20. Yamada Y, Beltran H. Clinical and biological features of neuroendocrine prostate cancer. *Curr Oncol Rep.* 2021;23(2):15. doi: 10.1007/s11912-020-01003-9
21. Kułakowski A. The contribution of Marie Skłodowska-Curie to the development of modern oncology. *Anal Bioanal Chem.* 2011;400(6):1583-1586. doi: 10.1007/s00216-011-4712-1
22. Borges de Souza P, McCabe CJ. Radioiodine treatment: an historical and future perspective. *Endocr Relat Cancer.* 2021;28(10):T121-T124. doi: 10.1530/ERC-21-0037
23. Salih S, Alkathheeri A, Alomaim W, Elliyanti A. Radiopharmaceutical treatments for cancer therapy, radionuclides characteristics, applications, and challenges. *Molecules.* 2022;27(16):5231. doi: 10.3390/molecules27165231
24. Tan H, Gu Y, Yu H. Total-body PET/CT: current applications and future perspectives. *AJR Am J Roentgenol.* 2020;215(2):325-337. doi: 10.2214/AJR.19.22705
25. Garg P, Singhal G, Horne D, Kulkarni P, Salgia R, Singhal SS. Molecular PET imaging: unlocking the secrets of cancer metabolism. *Biochem Pharmacol.* 2025;242:117202. doi: 10.1016/j.bcp.2025.117202
26. Sutherland DEK, Azad AA, Murphy DG, Eapen RS, Kostos L, Hofman MS. Role of FDG PET/CT in management of patients with prostate cancer. *Semin Nucl Med.* 2024;54(1):4-13.

- doi: 10.1053/j.semnuclmed.2023.06.005
27. Hirata K, Tamaki N. Quantitative FDG PET assessment for oncology therapy. *Cancers*. 2021;13(4):869.
doi: 10.3390/cancers13040869
 28. Shen Z, Li Z, Li Y, et al. PSMA PET/CT for prostate cancer diagnosis: current applications and future directions. *J Cancer Res Clin Oncol*. 2025;151(5):155.
doi: 10.1007/s00432-025-06184-z
 29. Rahman WT, Wale DJ, Viglianti BL, et al. The impact of infection and inflammation in oncologic 18F-FDG PET/CT imaging. *Biomed Pharmacother*. 2019;117:109168.
doi: 10.1016/j.biopha.2019.109168
 30. Gillett D, MacFarlane J, Bashari W, et al. Molecular imaging of pituitary tumors. *Semin Nucl Med*. 2023;53(4):530-538.
doi: 10.1053/j.semnuclmed.2023.02.005
 31. Schaafsma M, Berends AMA, Links TP, Brouwers AH, Kerstens MN. The diagnostic value of 18F-FDG PET/CT scan in characterizing adrenal tumors. *J Clin Endocrinol Metab*. 2023;108(9):2435-2445.
doi: 10.1210/clinem/dgad138
 32. Finessi M, Bisi G, Deandreis D. Hyperglycemia and 18F-FDG PET/CT, issues and problem solving: a literature review. *Acta Diabetol*. 2020;57(3):253-262.
doi: 10.1007/s00592-019-01385-8
 33. Kornberg A, Schernhammer M, Friess H. 18F-FDG-PET for assessing biological viability and prognosis in liver transplant patients with hepatocellular carcinoma. *J Clin Transl Hepatol*. 2017;5(3):224-234.
doi: 10.14218/JCTH.2017.00014
 34. Sheikh A, Anolik J, Maurer AH. Update on serum glucose and metabolic management of clinical nuclear medicine studies: current status and proposed future directions. *Semin Nucl Med*. 2019;49(5):411-421.
doi: 10.1053/j.semnuclmed.2019.06.001
 35. Van den Wyngaert T, Elvas F, De Schepper S, Kennedy JA, Israel O. SPECT/CT: standing on the shoulders of giants, it is time to reach for the sky! *J Nucl Med*. 2020;61(9):1284-1291.
doi: 10.2967/jnumed.119.236943
 36. Sgouros G, Bodei L, McDevitt MR, Nedrow JR. Radiopharmaceutical therapy in cancer: clinical advances and challenges. *Nat Rev Drug Discov*. 2020;19(9):589-608.
doi: 10.1038/s41573-020-0073-9
 37. Ren X, Zhang L, An R, Song H, Shi M, Wang Z. Focusing on prostate-specific membrane antigen in precision diagnosis and treatment of prostate cancer. *Biomedicines*. 2026;14(2):482.
doi: 10.3390/biomedicines14020482
 38. Iacovitti CM, Cuzzocrea M, Rizzo A, et al. Diagnostic value of dual-tracer PET/CT with [18F]FDG and PSMA ligands in prostate cancer: an updated systematic review. *Front Med (Lausanne)*. 2025;12:1607227.
doi: 10.3389/fmed.2025.1607227
 39. Hennrich U, Eder M. [68Ga]Ga-PSMA-11: the first FDA-approved 68Ga-radiopharmaceutical for PET imaging of prostate cancer. *Pharmaceuticals*. 2021;14(9):713.
doi: 10.3390/ph14080713
 40. Eder M, Schäfer M, Bauder-Wüst U, et al. 68Ga-complex lipophilicity and the targeting property of a urea-based PSMA inhibitor for PET imaging. *Bioconjug Chem*. 2012;23(4):688-697.
doi: 10.1021/bc200279b
 41. Ahmadzadehfar H, Seifert R, Afshar-Oromieh A, Kratochwil C, Rahbar K. Prostate cancer theranostics with 177Lu-PSMA. *Semin Nucl Med*. 2024;54(4):581-590.
doi: 10.1053/j.semnuclmed.2024.02.007
 42. Kratochwil C, Bruchertseifer F, Giesel FL, et al. 225Ac-PSMA-617 for PSMA-targeted α -radiation therapy of metastatic castration-resistant prostate cancer. *J Nucl Med*. 2016;57(12):1941-1944.
doi: 10.2967/jnumed.116.178673
 43. Kratochwil C, Haberkorn U, Giesel FL. 225Ac-PSMA-617 for therapy of prostate cancer. *Semin Nucl Med*. 2020;50:133-140.
doi: 10.1053/j.semnuclmed.2020.02.004
 44. Jeitner TM, Babich JW, Kelly JM. Advances in PSMA theranostics. *Transl Oncol*. 2022;22:101450.
doi: 10.1016/j.tranon.2022.101450
 45. Sun M, Niaz MJ, Niaz MO, Tagawa ST. Prostate-specific membrane antigen (PSMA)-targeted radionuclide therapies for prostate cancer. *Curr Oncol Rep*. 2021;23(5):59.
doi: 10.1007/s11912-021-01042-w
 46. Wester HJ, Schottelius M. PSMA-targeted radiopharmaceuticals for imaging and therapy. *Semin Nucl Med*. 2019;49(4):302-312.
doi: 10.1053/j.semnuclmed.2019.02.008
 47. Hu M, Zhang C, Fan D, Yang R, Bai Y, Shi H. Advances in preclinical research of theranostic radiopharmaceuticals in nuclear medicine. *ACS Appl Mater Interfaces*. 2025;17(3):4337-4353.
doi: 10.1021/acsami.4c20602
 48. Benešová M, Schäfer M, Bauder-Wüst U, et al. Preclinical evaluation of a tailor-made DOTA-conjugated PSMA inhibitor with optimized linker moiety for imaging

- and endoradiotherapy of prostate cancer. *J Nucl Med.* 2015;56(6):914-920.
doi: 10.2967/jnumed.114.147413
49. Weineisen M, Schottelius M, Simecek J, *et al.* 68Ga- and 177Lu-labeled PSMA I&T: optimization of a PSMA-targeted theranostic concept and first proof-of-concept human studies. *J Nucl Med.* 2015;56(8):1169-1176.
doi: 10.2967/jnumed.115.158550
 50. Umbricht CA, Benešová M, Schibli R, Müller C. Preclinical development of novel PSMA-targeting radioligands: modulation of albumin-binding properties to improve prostate cancer therapy. *Mol Pharm.* 2018;15(6):2297-2306.
doi: 10.1021/acs.molpharmaceut.8b00152
 51. Wang Z, Tian R, Niu G, *et al.* Single low-dose injection of Evans blue modified PSMA-617 radioligand therapy eliminates prostate-specific membrane antigen positive tumors. *Bioconjug Chem.* 2018;29(9):3213-3221.
doi: 10.1021/acs.bioconjchem.8b00556
 52. Liu T, Liu C, Xu X, *et al.* Preclinical evaluation and pilot clinical study of Al18F-PSMA-BCH for prostate cancer PET imaging. *J Nucl Med.* 2019;60(9):1284-1292.
doi: 10.2967/jnumed.118.221671
 53. Fu H, He H, Wang Y, *et al.* Preliminary evaluation of a novel PSMA-targeting radiopharmaceutical [68Ga]Ga/[177Lu]Lu-NYM032 for theranostic use in prostate cancer. *Eur J Nucl Med Mol Imaging.* 2025;52(5):1671-1684.
doi: 10.1007/s00259-024-07046-5
 54. Meyer C, Prasad V, Stuparu A, *et al.* Comparison of PSMA-TO-1 and PSMA-617 labeled with gallium-68, lutetium-177 and actinium-225. *EJNMMI Res.* 2022;12(1):65.
doi: 10.1186/s13550-022-00935-6
 55. Hu K, Li L, Huang Y, *et al.* Radiosynthesis and preclinical evaluation of bispecific PSMA/FAP heterodimers for tumor imaging. *Pharmaceuticals.* 2022;15(3):383.
doi: 10.3390/ph15030383
 56. Boinapally S, Lisok A, Lofland G, *et al.* Hetero-bivalent agents targeting FAP and PSMA. *Eur J Nucl Med Mol Imaging.* 2022;49(13):4369-4381.
doi: 10.1007/s00259-022-05933-3
 57. Wang X, Zhang X, Zhang X, *et al.* Design, preclinical evaluation, and first-in-human PET study of [68Ga]Ga-PSFA-01: a PSMA/FAP heterobivalent tracer. *Eur J Nucl Med Mol Imaging.* 2025;52(3):1166-1176.
doi: 10.1007/s00259-024-06965-7
 58. Wang P, Wang S, Liu F, *et al.* Preclinical evaluation of a fibroblast activation protein and a prostate-specific membrane antigen dual-targeted probe for noninvasive prostate cancer imaging. *Mol Pharm.* 2023;20(2):1415-1425.
doi: 10.1021/acs.molpharmaceut.2c01000
 59. Hou H, Gao J, Ma Y, *et al.* Development and biological evaluation of PSMA/FAP dual targeting radiotracers for prostate cancer imaging. *Inorg Chem Front.* 2024;11(19):6476-6485.
doi: 10.1039/D4QI01503G
 60. Wang Y, Li X, Li C, Xing H, Gao R, Jia B. A novel PSMA/FAP-specific radiotracer 99mTc-HFaPSMA for diagnosis of PSMA-negative prostate cancer: from preclinical validation to clinical translation. *J Med Chem.* 2025;68(16):17598-17610.
doi: 10.1021/acs.jmedchem.5c01294
 61. Liolios C, Bouziotis D, Sihver W, *et al.* Synthesis and preclinical evaluation of a bispecific PSMA-617/RM2 heterodimer targeting prostate cancer. *ACS Med Chem Lett.* 2024;15(11):1970-1978.
doi: 10.1021/acsmedchemlett.4c00324
 62. Mitran B, Varasteh Z, Abouzayed A, *et al.* Bispecific GRPR-antagonistic anti-PSMA/GRPR heterodimer for PET and SPECT diagnostic imaging of prostate cancer. *Cancers.* 2019;11(9):1371.
doi: 10.3390/cancers11091371
 63. Lundmark F, Abouzayed A, Mitran B, *et al.* Heterodimeric radiotracer targeting PSMA and GRPR for imaging of prostate cancer-optimization of the affinity towards PSMA by linker modification in murine model. *Pharmaceutics.* 2020;12(7):614.
doi: 10.3390/pharmaceutics12070614
 64. Jin W, Yan L, Li L, *et al.* PSMA and SSTR2 dual-targeting theranostic agents for neuroendocrine-differentiated prostate cancer (NEPC). *J Med Chem.* 2025;68(2):1984-1993.
doi: 10.1021/acs.jmedchem.4c02768
 65. Ma X, Wang M, Wang H, *et al.* Development of bispecific NT-PSMA heterodimer for prostate cancer imaging: a potential approach to address tumor heterogeneity. *Bioconjug Chem.* 2019;30(5):1314-1322.
doi: 10.1021/acs.bioconjchem.9b00252
 66. Schäfer M, Bauder-Wüst U, Leotta K, *et al.* A dimerized urea-based inhibitor of the prostate-specific membrane antigen for 68Ga-PET imaging of prostate cancer. *EJNMMI Res.* 2012;2(1):23.
doi: 10.1186/2191-219X-2-23
 67. Ruigrok EAM, van Vliet N, Dalm SU, *et al.* Extensive preclinical evaluation of lutetium-177-labeled PSMA-specific tracers for prostate cancer radionuclide therapy. *Eur J Nucl Med Mol Imaging.* 2021;48(5):1339-1350.
doi: 10.1007/s00259-020-05057-6

68. Gühne F, Radke S, Winkens T, *et al.* Differences in distribution and detection rate of the [68Ga]Ga-PSMA ligands PSMA-617, -I&T and -11-inter-individual comparison in patients with biochemical relapse of prostate cancer. *Pharmaceuticals*. 2021;15(1):9.
doi: 10.3390/ph15010009
69. Lau J, Jacobson O, Niu G, Lin KS, Bénard F, Chen X. Bench to bedside: albumin binders for improved cancer radioligand therapies. *Bioconjug Chem*. 2019;30(3):487-502.
doi: 10.1021/acs.bioconjchem.8b00919
70. Liu Z, Chen X. Simple bioconjugate chemistry serves great clinical advances: albumin as a versatile platform for diagnosis and precision therapy. *Chem Soc Rev*. 2016;45(5):1432-1456.
doi: 10.1039/c5cs00158g
71. Benešová M, Umbricht CA, Schibli R, Müller C. Albumin-binding PSMA ligands: optimization of the tissue distribution profile. *Mol Pharm*. 2018;15(3):934-946.
doi: 10.1021/acs.molpharmaceut.7b00877
72. Kramer V, Fernández R, Lehnert W, *et al.* Biodistribution and dosimetry of a single dose of albumin-binding ligand [177Lu]Lu-PSMA-ALB-56 in patients with mCRPC. *Eur J Nucl Med Mol Imaging*. 2021;48(3):893-903.
doi: 10.1007/s00259-020-05022-3
73. Cornelio DB, Roesler R, Schwartsmann G. Gastrin-releasing peptide receptor as a molecular target in experimental anticancer therapy. *Ann Oncol*. 2007;18(9):1457-1466.
doi: 10.1093/annonc/mdm058
74. Wang Q, Li Z, Huang Y, *et al.* A novel androgen-independent radiotracer with dual targeting of NTSR1 and PSMA for PET/CT imaging of prostate cancer. *Eur J Med Chem*. 2024;282:117050.
doi: 10.1016/j.ejmech.2024.117050